A novel multi-resolution technique for solving complex vorticity patterns in planar viscous flows past bodies through the DVH method

E. Rossi[a], D. Durante[b,*], S. Marrone[b], A. Colagrossi[b,c]

[a] *BCAM, Alameda Mazarredo 14, Bilbao, Spain*
[b] *CNR - INM, Via di Vallerano, Rome, Italy*
[c] *Ecole Centrale Nantes, LHEEA res. dept. (ECN and CNRS), Nantes, France*

Abstract

The Diffused Vortex Hydrodynamics (DVH) is a Vortex Particle Method widely validated in the last decade. This numerical approach allows cost-effective simulations of viscous flows past bodies at moderate and high Reynolds numbers, by taking into account only the rotational part of the flow field. In the present work a novel multi-resolution technique is presented in order to limit the number of particles in the computational domain, further improving the solver efficiency. The proposed technique preserves the total circulation and uses the Benson et al. (1989) deterministic algorithm to regularize the particle spatial distribution during the diffusion step. Simulations of the planar flow past five cylindrical sections at Re $= 10,000$ are discussed: flat plate, triangle, square, circular cylinder and a symmetrical airfoil. Although the simulations are carried out in a two-dimensional framework, complex vorticity patterns develop because of the flow separation and the Reynolds number considered. Comparisons with a Finite Volume solver are carried out and discussed, such highlighting the advantages of the present numerical approach.

Keywords: Vortex Particle Method, Diffused Vortex Hydrodynamic (DVH), viscous flow past a body, multi-resolution, Vortex wake dynamics.

1. Introduction

The study of planar flows is of great importance in a wide class of problems where stratified conditions take place as, for example, in meteorological forecasting or in free surface flows where the Reynolds numbers are high and the Froude numbers are very small.

The experimental investigation of planar flows can benefit from the improvements of the flowing soap film apparatuses combined with the use of a high-speed camera and low-

*Corresponding author
Email address: danilo.durante@cnr.it (D. Durante)

pressure sodium lamp, thus allowing the visualization of complex interference patterns (Fayed et al., 2011). These kinds of experimental devices are also used for the visualization of the vortex wake of a flapping foil (Schnipper et al., 2009) or of a flexible filament subject to forced vibrations (Jia et al., 2015). Thanks to these recent experimental developments, many numerical studies on planar flows past fixed, moving or deformable frontiers can be found in the recent literature (see, for example, Reichl et al. (2005); Das et al. (2016); Krishnan et al. (2016); Ye et al. (2017); Badrinath et al. (2017); Bose and Sarkar (2018); Mandujano and Málaga (2018); Colagrossi et al. (2019)).

Planar viscous flows are also considered for the chaotic transition of two-dimensional dynamical systems, see *e.g.* Pulliam and Vastano (1993); Kurtulus (2015, 2016); Rossi et al. (2018); Durante et al. (2020, 2021). In those cases, the flow separation is responsible for the shedding of vortex structures which lead to the generation of complex wake patterns in the far field.

The numerical simulations of viscous flow past a body at Reynolds numbers Re $\geq 10^4$ generate complex wake fields even in a two dimensional framework and, for this reason, they require significant computational resources for resolving all the vorticity scales within the numerical domain. Because of this, the solution of these kinds of flows by means of mesh-based methods presents severe limitations due to the high computational costs.

In order to accurately resolve the flow field inside the regions of interest, a Chimera overlapping grid approach proves to be a good compromise between accuracy and computational costs (see *e.g.* Muscari (2005); Muscari et al. (2006)). However, since the regions where the gradients are higher are not known *a priori*, the main drawback remains the overestimation of the total number of mesh elements.

The adaptive mesh refinement (AMR) technique, widely exploited nowadays, may help in confining the mesh cells' clustering to domain subsets where higher gradients appear, thus allowing to resolve with a high level of detail both the near and the far fields. As a main drawback, the AMR algorithms are not easy to implement and parallelize on clusters or GPUs (see Hannoun and Alexiades (2007)). Furthermore, in order to allow a well balanced parallelization, an immersed boundary approach may be the best option for taking into account the presence of bodies within the flow field (see Rossinelli et al. (2015)). This strategy, although numerically efficient, represents a significant hindrance for the description of complex geometries, as outlined in Cohen (2002).

Simulations of planar flows past solid bodies are easier by means of Vortex Particle Methods (VPMs). With this technique the governing equations are solved with a Lagrangian formulation: the velocity field is first evaluated through a Fast Multiple Method (FMM) (see Yokota and Barba (2013)) for the Poisson equation and then used to move the vortex particles in the numerical domain. The advantage of this approach is that the VPM can be formulated in a pure meshless framework and that the boundary layer regions can be described in a body-fitted fashion, such overcoming the drawbacks of immersed boundary methods. Furthermore, the Lagrangian formulations ensure accurate computations of the advection term, by avoiding the discretization of the non-linear term. As a drawback, the Lagrangian approach leads to uneven spatial distributions with rarefaction or clusterization of the particles that eventually worsen the global accuracy of the numerical simulations (see *e.g.* Barba et al. (2003)).

A possible remedy to this problem is the particle redistribution technique, which consists in the interpolation of the vorticity field on a regular mesh (see *e.g.* (Shankar and Van Dommelen, 1996), (Barba, 2005).

In the present work, a recently developed VPM called Diffused Vortex Hydrodynamics (DVH) is considered (for details see also (Rossi et al., 2015a,b, 2016; Colagrossi et al., 2016)). The DVH is a meshless method that uses the operator splitting technique introduced by Chorin (1973), which consists in a stepped solution of the Helmholtz vorticity equation. The time evolution of the vorticity field is subdivided in two sub-steps: a pure advection and a pure diffusion. For the advection, the velocity field is evaluated through a FMM (see *e.g.* Graziani and Landrini (1999)), whereas the diffusion is performed on regular point lattices, by considering a superposition of elementary heat equation solutions as explained in Benson et al. (1989). The no-slip boundary conditions are enforced through the generation of a vortex sheet, as clarified in Chorin (1973) and in Giannopoulou et al. (2019). The DVH is also coupled to a packing algorithm (Colagrossi et al., 2012) exploited for building a "Regular Point Distribution" (RPD) fitted to a solid surface. This procedure is computationally cheap and arranges lattice points around complex contours by maintaining their relative distance approximately constant. Thanks to this algorithm, the DVH calculations are body-fitted even when complex body shapes are involved.

In order to fulfill the no-slip boundary conditions, new vortices are generated on the body surface at every time step; hence, the total number of vortices within the flow field may rise as much as to become computationally unfeasible. In order to overcome this issue, a new multi-resolution algorithm is introduced in the present work. The flow field is split in sub-domains where the particle size is reduced while moving away from the body. In this way it is possible to control and limit the total number of vortex particles also for long simulations. This technique demonstrates to be a good trade off between accuracy and computational time.

In order to challenge the multi-resolution algorithm with complex flows, five different geometries at Re=10,000 are investigated. Blunt and sharp surfaces are taken into account and the results are compared with a Finite Volumes mesh-based solver. In particular, in four cases an in-house solver (called *Xnavis*) was used. Some key features of this solver are outlined in section 4.

As explained in the following sections, the wide range of resolved vortex scales makes the simulations presented in this work excellent candidates for comparative or benchmarks investigations.

The present article is structured as follows:

- Section 2 contains a description of the DVH method together with a remark on the choice of diffusive and advective time steps;
- Section 3 presents the new multi-resolution algorithm;
- Section 4 briefly recalls the main features of the Xnavis solver.
- Section 5 contains the discussion of the flow past five different geometries and the comparison with the FVM Xnavis.

Conclusions wrap up the paper.

2. A brief recall of the Diffused Vortex Hydrodynamics (DVH) method.

In the present work the fluid is considered incompressible and its motion governed by the two dimensional Navier-Stokes written in vorticity formalism:

$$\frac{D\omega}{Dt} = \nu\,\Delta\omega \qquad \forall \mathbf{r} \in \Omega, \tag{1}$$

where D/Dt is the material derivative, ω is the vorticity, ν is the kinematic viscosity and Ω is the fluid domain.

In order to solve eq. (1), at each time step the operator splitting scheme (Chorin, 1973, 1978) is used subdividing each time step of the numerical integration in two sub-steps. The first consists in an inviscid advective step governed by the Euler equation:

$$\left\{ \begin{array}{rcl} \dfrac{D\omega}{Dt} & = & 0 \\ \dfrac{D\mathbf{r}}{Dt} & = & \mathbf{u}(\mathbf{r}, t) \\ \nabla^2\mathbf{u} & = & -\mathrm{curl}(\boldsymbol{\omega}),\ \boldsymbol{\omega} = \omega\,\mathbf{e}_3\,, \end{array} \right. \tag{2}$$

where $\mathbf{e}_3$ is the unit vector along the z direction. The advective step is followed by a diffusive sub-step governed by the heat equation:

$$\frac{\partial}{\partial t}\omega(\mathbf{r}, t) = \nu\Delta\omega(\mathbf{r}, t). \tag{3}$$

The vorticity field is discretised as a sum of N vortices, each of them represented by a positive smooth approximation of the Dirac δ distribution, δ_ϵ, and a circulation Γ_i:

$$\omega(\mathbf{r}, t) = \sum_{i=1}^{N} \Gamma_i(t)\delta_\epsilon(\mathbf{r} - \mathbf{r}_i). \tag{4}$$

Each vortex particle is advected by the velocity field during the advection step (2). The particle Lagrangian motion may induce excessive clustering or rarefaction of the particles distribution during their evolution, leading to a poor vorticity evaluation when using equation (4). To avoid this problem, in the DVH model "Regular Point Distributions" (RPDs) are used during the diffusive step. RPDs are sets of almost equispaced points without any topological connection between each other. During the diffusive step, each vortex particle is associated with a specific RPD and gives vorticity contributions to these points using the elementary solution of the heat equation, following the deterministic algorithm described in Benson et al. (1989). This special set of points will then become the new set of vortex particles overwriting the previous one. This procedure prevents the excessive clustering or rarefaction of the vortex particles, and avoids the remeshing procedure which would be required otherwise (see e.g. Barba et al. (2003)).

2.1. Generation of the Regular Point Distributions (RPDs)

RPDs around bodies are generated using the packing algorithm described in Colagrossi et al. (2012) allowing to arrange points around complex shapes preserving the volume around each point. This algorithm places the points around the body on a regular (Cartesian) mesh with constant spacing Δr, while the packing algorithm, using a simple particle-interaction model, rearranges the points around the body preserving the volume around each point.

An example of RPD generated around a solid body can be seen in Fig. 1. It is worth noting that the distribution of points generated can be not symmetric even for symmetric bodies, meaning that symmetries in the RPD should be explicitly enforced, if needed. The small asymmetries present in the RPD distribution may trigger the vortex shedding without the necessity to perturb the flow field during the transient stage as discussed in section 5.

Far from the solid body simple Cartesian meshes are used as RPDs. The multi-resolution algorithm allows the introduction of sub-domains in the wake region where the resolution can be coarsened while moving downstream. The a detailed discussion of the multi-resolution can be found in section 3.

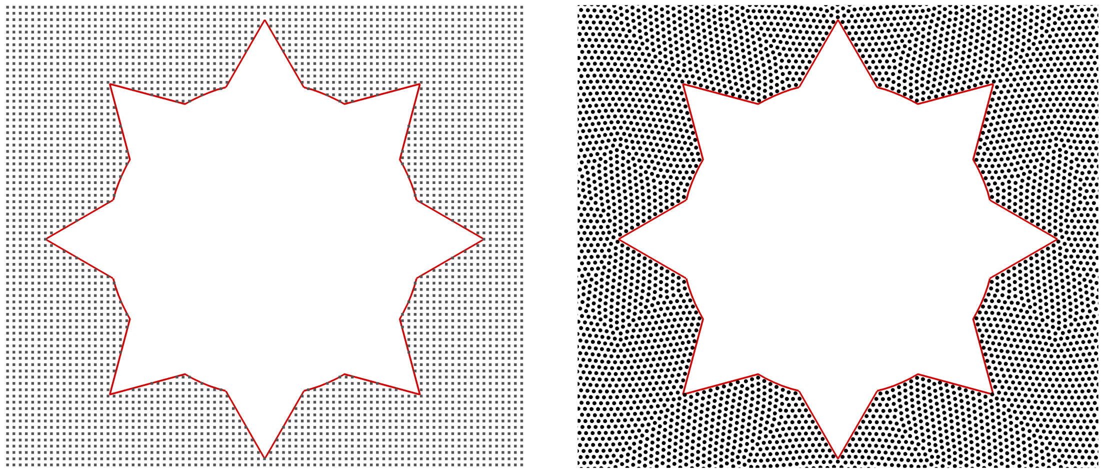

Figure 1: Un-Packed (**left**) Vs Packed (**right**) configurations around a composed object.

2.2. *Advection step: velocity field evaluation and enforcement of the no-slip boundary conditions*

Following the Helmholtz–Hodge Decomposition (HHD) theorem, the velocity field can be split into a curl-free and a divergence-free component:

$$\mathbf{u} \;=\; \nabla\phi \;+\; \nabla\times\Psi \;=\; \mathbf{u}_\infty \;+\; \mathbf{u}_\phi \;+\; \mathbf{u}_\omega \tag{5}$$

where the curl-free component is given by the sum of the free stream velocity $\mathbf{u}_\infty$ and the velocity induced by presence of the body $\mathbf{u}_\phi$. The velocity induced by the vortex particles is indicated with $\mathbf{u}_\omega$ and can be evaluated using the Biot-Savart law:

$$\mathbf{u}_\omega(\mathbf{r},t) = \sum_{i=1}^{N} \Gamma_i(t)\,\mathbf{K}_\epsilon(\mathbf{r},\mathbf{r}_i) \tag{6}$$

where $\mathbf{K}_\epsilon$ is the mollified Biot-Savart kernel. Evaluation of equation (6) are sped up through a classic FMM (see *e.g.* Graziani and Landrini (1999)).

$\mathbf{u}_\phi$ is evaluated through an indirect Boundary Element Method (BEM) discretizing the body surface with a set of N_b element of length Δs. Each element represents a source with strength σ_j and a point vortex with circulation γ_j:

$$\mathbf{u}_\phi(\mathbf{r},t) = \sum_{j=1}^{N_b}\Big[\mathbf{K}_\epsilon(\mathbf{r},\mathbf{r}_j)\times\mathbf{e}_3\Big]\,\sigma_j\,\Delta s \;+\; \sum_{j=1}^{N_b}\Big[\mathbf{K}_\epsilon(\mathbf{r},\mathbf{r}_j)\Big]\,\gamma_j\,\Delta s \;\;. \tag{7}$$

In equation (7) the source strengths and circulations are both unknown. In order to evaluate them, a two-step procedure is followed: the impermeability condition is enforced first on the body surface followed by the no-slip condition. In the first step the circulations γ_j are assumed constant and equal to

$$\hat{\gamma}(t) = -\frac{\Gamma(t) - \Gamma_\infty(t)}{\mathcal{P}}, \tag{8}$$

where $\mathcal{P}$ is the perimeter of the body, $\Gamma(t)$ is the total circulation in the fluid domain at time t (*i.e.* $\Gamma(t) = \sum_i \Gamma_i(t)$) and $\Gamma_\infty(t)$ is the circulation at infinity. For all the problems addressed in the present paper $\Gamma_\infty \equiv 0$.

Substituting the relation (8) in (7) we get:

$$\mathbf{u}'_\phi(\mathbf{r_i}, t) = \left[\sum_{j=1}^{N_b} [\mathbf{K}_\epsilon(\mathbf{r_i}, \mathbf{r}_j) \times \mathbf{e}_3]\, \Delta s\right] \sigma_j + \left[\sum_{j=1}^{N_b} \mathbf{K}_\epsilon(\mathbf{r_i}, \mathbf{r}_j)\, \Delta s\right] \hat{\gamma}_j \tag{9}$$

Assuming σ_j constant on each panel, it is possible to enforce the impermeability condition using the equation (9) and projecting the decomposition (5) along the body normal, obtaining the following algebraic system:

$$\mathbb{A}_{ij}\,\sigma_j = -\mathbf{u}_\infty \cdot \mathbf{n}_j - \mathbf{u}_{\omega j} \cdot \mathbf{n}_j + \mathbb{B}_{ij}\,\hat{\gamma}_j \qquad i, j = 1, \ldots, N_b \tag{10}$$

where $\mathbb{A}$ and $\mathbb{B}$ are squared $N_b \times N_b$ matrices. σ_j is then the solution of system (10) with the aforementioned assumption (8).

After the computation of the sources, the distribution of γ_j is computed by enforcing the no-slip condition according to Chorin (1978). It is worth noting that this distribution generates a velocity component that cancels out the tangential velocity on the body:

$$\gamma_j = -\mathbf{u}_\infty \cdot \boldsymbol{\tau}_j - \mathbf{u}_{\omega j} \cdot \boldsymbol{\tau}_j + \mathbb{A}_{ij}\hat{\gamma}_j + \mathbb{B}_{ij}\,\sigma_j \qquad j = 1, \ldots, N_b \tag{11}$$

where $\boldsymbol{\tau}$ is the anticlockwise tangent unit vector on the body surface.

The velocity $\mathbf{u}$ is then used to advect the vortex particles with a fourth-order Runge-Kutta time integration, where each vortex particle maintains its initial circulation:

$$\begin{cases} \dfrac{d\Gamma_i}{dt} = 0 \\[2ex] \dfrac{d\mathbf{r}_i}{dt} = \mathbf{u}(\mathbf{r}_i, t) \\[2ex] \mathbf{u} = \mathbf{u}_\infty + \mathbf{u}_\omega + \mathbf{u}_\phi \end{cases} \tag{12}$$

The interested reader is addressed to Rossi et al. (2015a); Giannopoulou et al. (2019) for further details.

2.3. Diffusive step

During the diffusive step, the heat equation (3) is solved using the deterministic algorithm described in Benson et al. (1989): each vortex particle gives a vorticity contribution on RPDs by a superposition of elementary solutions of the heat equation, giving the vorticity field:

$$\omega(\mathbf{r}, t) = \sum_{i=1}^{N} \frac{\Gamma_i(t)}{4\pi\nu\Delta t_d} \exp\left[-\frac{|\mathbf{r} - \mathbf{r}_i(t)|^2}{4\nu\Delta t_d}\right] \mathcal{H}[R_d - |\mathbf{r} - \mathbf{r}_i(t)|] \tag{13}$$

where $\mathcal{H}[\cdot]$ is the Heaviside function, Γ_i and $\mathbf{r}_i$ are the circulation and the position of the i-th vortex at time t, Δt_d is the diffusive time step and R_d, called the diffusive radius, is the distance at which the Gaussian distribution is truncated for numerical purposes (see Rossi et al. (2015b, 2016)). The following expression relates the ratio $R_d/\Delta r$ to the number of RPD nodes N_{node} inside the diffusive radius:

$$N_{node} = \left\lfloor \pi \left(\frac{R_d}{\Delta r}\right)^2 \right\rfloor \tag{14}$$

where $\lfloor\cdot\rfloor$ is the floor function. A typical number for N_{nodes} for 2D simulations is 51 corresponding to a ratio $R_d/\Delta r = 4$. It is important to highlight that N_{node}, and consequently the ratio $R_d/\Delta r$, together with Δr are the two key discretization parameters for the DVH model. Detailed convergence studies varying these parameters can be found in Rossi et al. (2015b).

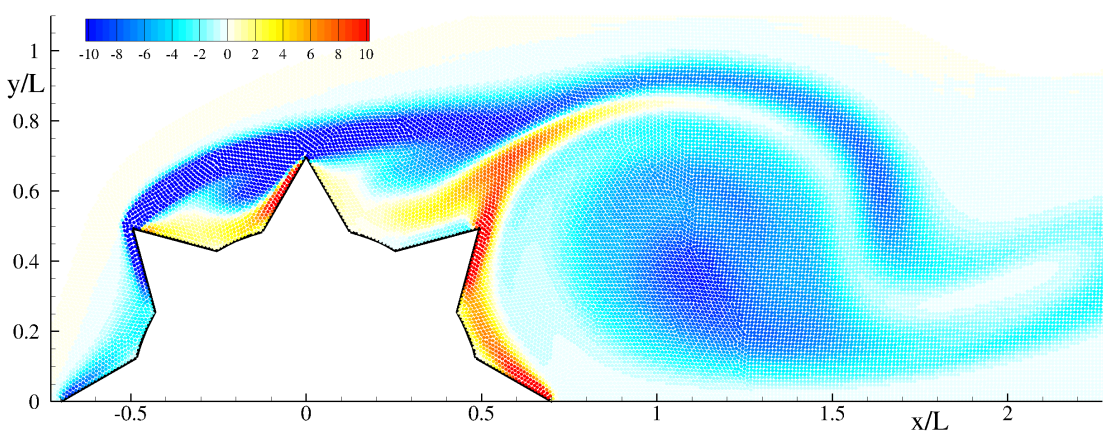

Figure 2: Flow past a composed object. Flow current from left to right with intensity U at Reynolds number $\mathrm{Re} = UL/\nu = 1000$. The colors are representative of the dimensionless vorticity field $\omega L/U$ (red anticlockwise, blue clockwise) at time instant $tU/L = 6$. Vorticity is diffused on the RPD shown on fig. 1 .

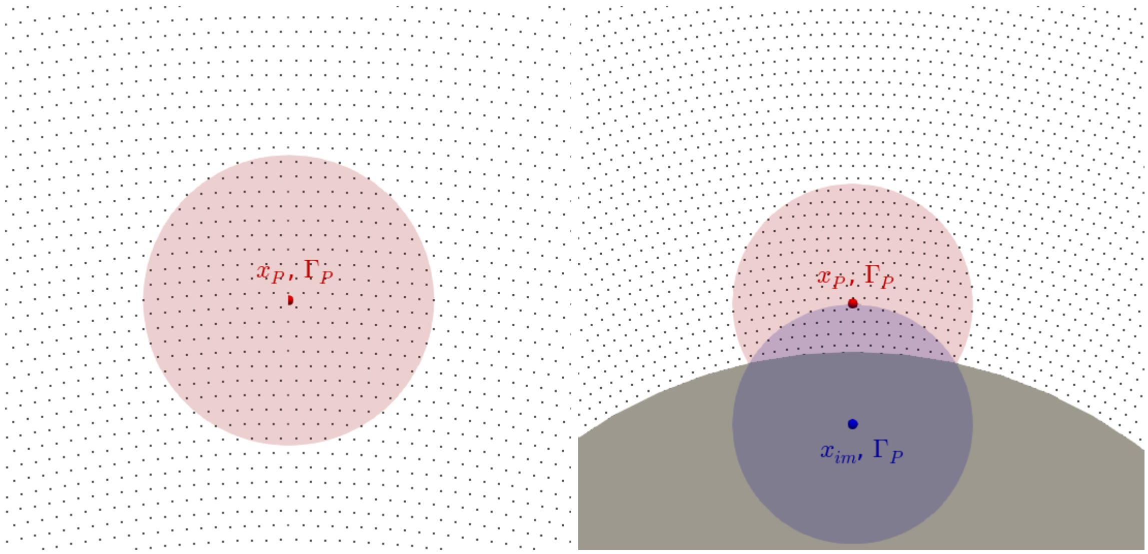

Figure 3: Left: Diffusion in free space. Right: Diffusion in presence of a solid boundary.

The set of points created during the diffusion process become the new set of vortex particles overwriting the previous one. The use of RPDs during diffusion impedes the excessive clustering or rarefaction of the vortex particles, avoiding remeshing procedures.

Fig. 2 shows the vorticity field evaluated using the RPDs for the flow past a composed object. The vorticity is evaluated using the particles circulation Γ_i, generated during the diffusive step, through equation (13).

A sketch of the diffusion of a single point vortex in free space can be seen in the left plot of Fig. 3.

In order to solve the diffusion near a smooth solid boundary, a homogeneous Neumann condition for the vorticity field, together with a flat plate approximation of the solid contour, will be used: for every vortex with a distance from a solid contour less than R_d an image vortex inside the body is created symmetrically along the direction of the local normal. The contribution to the vortex diffusion is now taken into account by diffusing the image vortex, hence reflecting inside the domain the otherwise outgoing vorticity. A sketch of the diffusion of a single point vortex in presence of a solid boundary can be seen in right plot of Fig. 3.

This approximation is no longer valid for bodies with geometrical singularities. In this case a suitable visibility mask must be introduced, as explained in Rossi et al. (2016).

2.4. Choice of diffusive and advective time steps

The DVH method uses the operator splitting scheme, solving the vorticity field evolution in two steps: advection and diffusion. For this reason two different time steps have been introduced in the DVH method: advective Δt_a and diffusive Δt_d time steps.

Considering U and L as the reference velocity and length of the problem, the Reynolds number is defined as $\mathrm{Re} = UL/\nu$.

According to the derivation described in Rossi et al. (2015a), each RPD can be associated to a specific diffusive time step Δt_d, depending on the Reynolds number chosen for the study as well as on the specific RPD spatial resolution $L/\Delta r$:

$$\Delta t_d \frac{U}{L} \simeq 0.34 \frac{\mathrm{Re}}{(L/\Delta r)^2}, \tag{15}$$

The advective time step Δt_a can be chosen by considering both the flow velocity U and the discretization Δr:

$$\Delta t_a \frac{U}{L} = \mathrm{Co} \frac{1}{(L/\Delta r)} \tag{16}$$

where the Courant number Co is $O(10^{-1})$ in order to avoid too large particles displacements with respect to the particle spacing.

During a time interval Δt_d, more than one advection step can be performed. This is true especially far from the boundary layer regions, where coarser spatial discretizations are used.

In order to synchronize diffusion and advection steps, Δt_a and Δt_d are in integer ratio, meaning that Δt_a is rearranged in the following way:

$$N_{\Delta t} = \left\lfloor \frac{\Delta t_d}{\Delta t_a} \right\rfloor \rightarrow \Delta t_a = \frac{\Delta t_d}{N_{\Delta t}} \tag{17}$$

This correction can be interpreted as a modification of the Courant number used during the simulation with respect to the one initially introduced. Equation (17) highlights that, in order to complete a splitting step, a vortex has to perform a specific amount of advective time steps equal to the diffusion time step duration.

3. A novel multi-resolution algorithm for the DVH method

The present DVH method adopts a novel multi-resolution technique in order to simulate long vortex wakes generated by the flows past bodies. The multi-resolution is obtained with the superposition of domains with different spatial discretization.

An example of multi-resolution is given in figure 4, where each domain used is represented with a different color. The packing algorithm is used for generating the RPD in the closest body domain only, while in the other domains the points arrangements are simply uniform Cartesian lattices. In order to balance accuracy and computational costs, the further downstream the domain is, the coarser the resolution (typically halved at every domain change).

Each domain is characterized by its own spatial discretization Δr, a diffusive time step Δt_d described by equation (15) and a diffusive radius R_d. Each domain will perform a diffusive step every Δt_d which means that all the vortex particles lying within its boundaries have to perform a diffusive step on the underlying RPD. It is important to note that the advective time step Δt_a is the same for all the RPD used and is evaluated by considering the smallest Δr adopted in the simulation. Furthermore, each domain is associated to a specific *extension*, which is crucial for the diffusion of vortices moving across two adjacent domains.

To better explain the transition of a vortex from a domain to another, two different domains, A and B, with two different spatial resolutions such that $\Delta r_A < \Delta r_B$, are here considered. Note that if $\Delta r_A < \Delta r_B$, then also $\Delta t_{dA} < \Delta t_{dB}$ and $R_{dA} < R_{dB}$. Moreover, in order to assure that the operating splitting scheme is correctly applied in each domain, the definition (17) should hold for each different domain, meaning that

$$\frac{\Delta t_{dA}}{\Delta t_a} = N_{\Delta t_A} \neq N_{\Delta t_B} = \frac{\Delta t_{dB}}{\Delta t_a} \tag{18}$$

In order to simplify the multi-resolution algorithm, all the $N_{\Delta t}$ are in integer ratio, N_{AB},

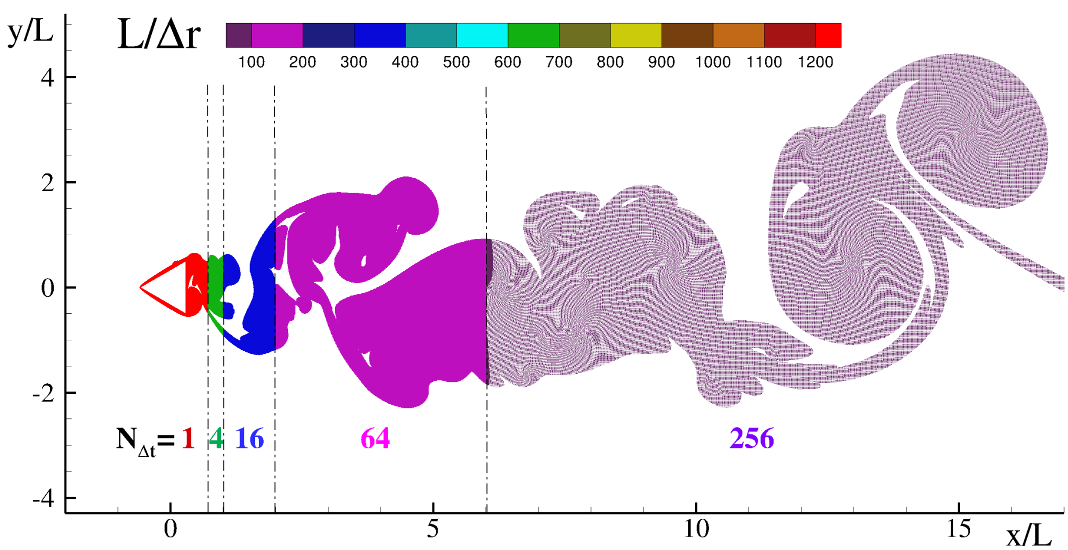

Figure 4: Example of multi-resolution simulation using different RPDs with decreasing resolution.

with each other:

$$\frac{\Delta t_{dB}}{\Delta t_{dA}} = \frac{N_{AB} N_{\Delta t_A}}{N_{\Delta t_A}} \rightarrow \Delta r_B = \sqrt{N_{AB}} \Delta r_A \tag{19}$$

where we have used the relations (15) and (17).

Domain discretization is halved while changing domain in the streamwise direction, in order to avoid too large differences between diffusive time steps of adiacent domains, thus setting $\Delta r_B = 2\Delta r_A$ and $N_{AB} = 4$.

It is important to highlight that also the diffusive radius R_d changes while changing the resolution. The ratio $R_d/\Delta r$ and the number of RPD nodes N_{node} is kept constant during the simulation and throughout the computational domain, therefore, as shown by equation (14), R_d grows linearly with Δr. In our example, when passing from domain A to domain B the ratio of the diffusive radii will be $R_{dB}/R_{dA} = 2$.

To understand the effect of the multi-resolution technique, it is useful to analyse what happens to a single vortex moving downstream in the wake past a solid body. Usually, a vortex particle generated on domain A moves along the wake during its advection until it undergoes diffusion, after $N_{\Delta t_A}$ iterations. At that point two possible scenarios may arise: the vortex particel still lies in domain A, where it was generated, or it moved to domain B. In the first scenario the vortex particle will diffuse, as described in section 2.3, on the RPD of domain A with Δt_{dA} as diffusive time step. If the vortex is near the boundary of domain B, i.e. its distance from the domain frontier is less then R_{dA}, an extension of domain A at least equal to R_{dA} is used to generate vortices falling beyond the frontier with domain B. This strategy avoids the diffusion of a single vortex on RPDs with different discretizations and it guarantees the same diffusion process accuracy close to domains boundaries.

In the second scenario, the vortex generated in domain A cross the boundary with domain B before it is ready to diffuse (*Case 1*). It is important to note that a vortex particle can also cross a domain boundary in the other direction, i.e. a vortex generated in domain B (with coarser resolution) can move to domain A before it is ready to diffuse (*Case 2*).

Note that, when the diffusive step is performed in domain B the same happens also for domain A, whereas vice versa does not hold always true, being $N_{\Delta t_B} = 4N_{\Delta t_A}$.

Considering *Case 1*, two possible scenarios can take place depending on the number of time steps elapsed from the vortex generation:

- **Case 1a)** The vortex moves from domain A to domain B and only domain A is ready to diffuse while it is not the case for domain B. In this situation an extension of domain A will be introduced in order to allow for the vortex diffusion, using Δt_{dA} and R_{dA} as diffusive time step and diffusive radius respectively, as shown in the left plot of figure 5. In bottom left plot of figure 5, a one dimensional representation of the Gaussian distribution used for the diffusion process together with the RPD of

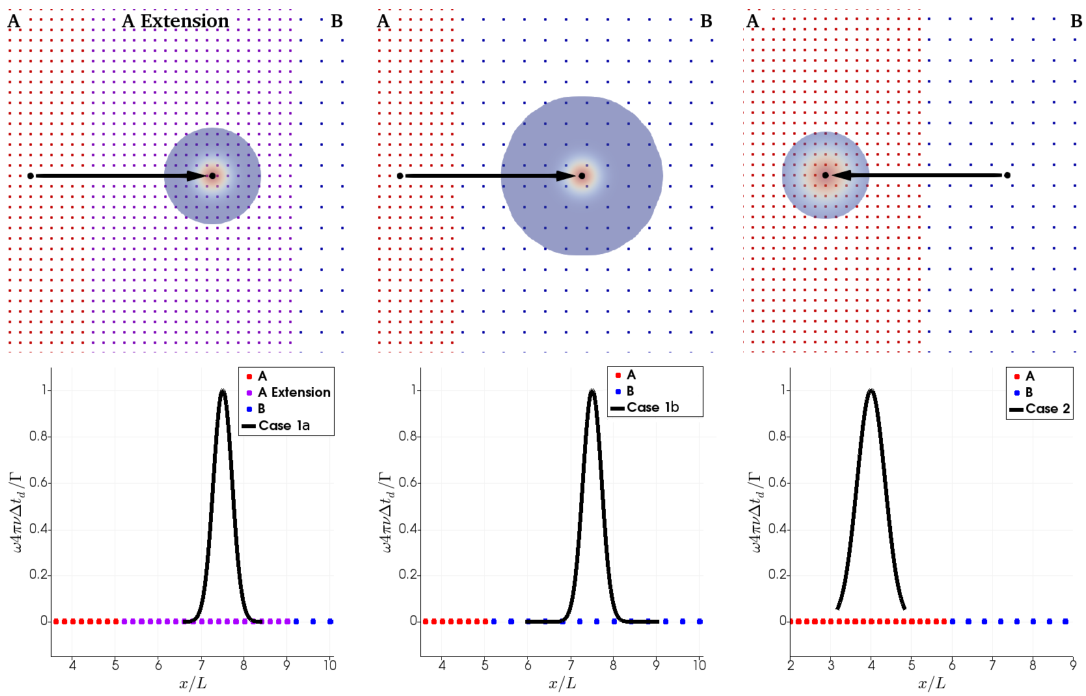

Figure 5: Left: diffusion on domain A using the domain extension (Case 1a). Center: diffusion on domain B of vortices generated on domain A for which $n\Delta t_a < N_{\Delta t_{dB}}$ (Case 1b). Right: diffusion on domain A of vortices generated on domain B for which $n\Delta t_a > N_{\Delta t_{dA}}$ (Case 2).

the two domains and the domain extension are depicted. The Gaussian distribution have been truncated at a distance R_{dA} from its center. The new generated vortices are classified as still generated in domain A and they will continue to diffuse according to Δt_{dA} until domain B will be ready to diffuse. The width of the domain extension is therefore calculated each time by considering the positions of the outermost vortex still belonging to the domain A. The extension is needed to avoid too large deformation of the vortex distribution between two consecutive diffusion steps. It is worth noting that this scenario occurs when $R_{dA} < R_{dB}$.

- **Case 1b)** The vortex moves from domain A to domain B and both domains are ready to diffuse. In this case all vortices insisting on domain B have to perform diffusion, including the ones generated on domain A or on its extension (as in *Case 1a*), even if the number of iterations $n < N_{\Delta t_{dA}}$ performed from their generation is lower than $N_{\Delta t_{dB}}$. In this case, vortices diffuse on the RPD of domain B, following the same algorithm described in section 2.3, using R_{dB} as diffusive radius but a different diffusive time step:

$$\Delta t_d = n\, \Delta t_a \tag{20}$$

where n is the number of advective time steps performed from the generation of each vortex. A sketch of this case is depicted on the top and bottom center plots of figure 5.

- **Case 2** In this situation, a vortex generated in domain B moves to domain A. In this case the number of iterations n performed from its generation is such that $n \geq N_{\Delta t_{dA}}$. Similarly to *Case 1b*, this vortex diffuses on the RPD of domain A using R_{dA} as diffusive radius but the diffusive time step will be given by equation (20). In the particular case in which $n = N_{\Delta t_{dA}}$, we have $\Delta t_d = \Delta t_{dA}$. A sketch of this case is depicted on the top and the bottom right plots of figure 5.

The Reynolds number of the problem is the crucial parameter correctly chose the RPDs number, size and resolution. In fact, the vorticity structures shed in the flow field becomes smaller while increasing the Reynolds number, as described, for example, in Durante et al. (2017) while studying the flow past a circular cylinder. This implies that the RPD with the highest resolution should be placed around the body in a body-fitted fashion and its resolution has to be set in such a way that $\mathrm{Re}_{\Delta r} = \mathcal{O}(1)$, where $\mathrm{Re}_{\Delta r}$ is the cell Reynolds number, *i.e* $\mathrm{Re}_{\Delta r} = U \Delta r / \nu$. In this way the algorithm is able to capture even the smallest vortex scales of the flow similarly to a Direct Numerical Simulation (DNS). In order to limit the computational costs, the RPD resolution is progressively reduced away from the body exploiting the multi-resolution approach described above. This coarsening does not affects the quality of the simulation: the inverse energy cascade, characteristic of 2D problems, induces the coalescence of small vortices into larger ones whose evolution can be accurately simulated with coarser resolutions.

It is worth mentioning that the FMM algorithm used for the velocity field evaluation, is not influenced by the presence of multiple domains with different resolutions, as outlined also in Colagrossi et al. (2016); Rossi et al. (2015a). In order to assess the reliability of the multi-resolution algorithm, an analysis of the flow past a circular cylinder at Re=1000 is performed in AppendixA, where the comparison between a uniform and a multi-resolution flow field is carried out. Moreover, in AppendixB a convergence study related to the multi resolution approach is performed and the convergence rate is estimated.

4. Brief recall of the FVM code

Xnavis is a general-purpose finite volume, multi-block structured mesh solver, developed at CNR-INM (formerly CNR-INSEAN). In this solver the Navier-Stokes equations are approximated by a finite volume technique with pressure and velocity co-located

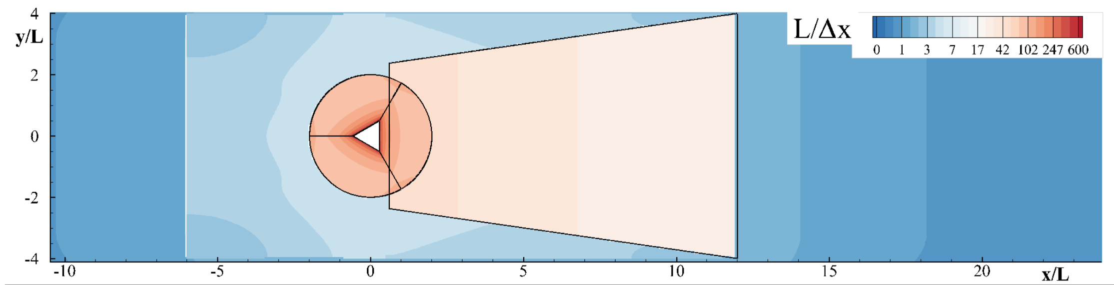

Figure 6: Example of a Chimera overlapped grids technique used with the current FVM code. Different topologies are highlighted with black edges. The field of the characteristic cell dimension (*i.e.* the square root of area) inverse is drawn for highlighting the mesh stretching and the resolution of the different blocks. For the sake of clearness, only the near body area is magnified and the contour color scale is logarithmic.

at the cell center. In this section the 2D version of this solver is briefly described. The interested reader may also refer to Di Mascio et al. (2001); Muscari (2005); Muscari et al. (2006); Broglia et al. (2014); Broglia and Durante (2018) for a more detailed discussion.

The residual on each control volume is computed as an interface flux balance; the fluid domain Ω is partitioned into N_l adjacent or overlapping blocks Ω^l, each one subdivided into $N_i \times N_j$ disjoint hexahedrons Ω^l_{ij}.

Conservation laws are applied to the control volume (i, j), whereas the surface integrals are evaluated by means of a second order formula. The velocity gradients computation, required to evaluate the stress tensor at the cell interface, is performed using a standard second order centered finite volume approximation (Hirsch, 2007).

A pseudo-compressible approach is adopted for the pressure field evaluation, in order to avoid the direct resolution of the related Poisson equation. The evolution at every time step is obtained in the form of a pseudo-time steady condition using a three-points backward second order formula. Grid refinement/coarsening have been introduced in the numerical computations presented in this paper using overlapping grid. The overlapping grid approach (or "Chimera" method) implemented in Xnavis is obtained through a modification of both the boundary conditions and the internal point treatment for those zones where the overlapping occurs. An example of the overlapping grids designed for the present simulations is sketched in figure 6. The approach is based on the search of the "donors" (the set of cells *donating* the solution) in those cells ("chimera cells") for which an overlap is found. Once the donors are identified, a convex set of eight donor cell centers is searched and a trilinear interpolation is used to transfer the solution from the "donor" set to the "chimera" cell. Differently from standard chimera approaches, however, the cells marked as "chimera" are not removed from the computation, but the interpolated solution is enforced by means of a forcing term added in the Navier–Stokes equations in a "body-force" fashion. For more details, the interested reader may refers to Muscari (2005) and Muscari et al. (2006).

5. Flows at Re=10,000 around five different cylindrical sections

In this section the flow past five different geometries at Re $= 10,000$ is analysed. In particular, the study is focused on a transverse flat plate, a triangular, a squared and a circular cylinder and a NACA0012 airfoil at several angles of attack. The reference length for the various geometries is indicated with c: the length of the plate, the side of the equilateral triangle, the side of the square, the diameter of the cylinder and, finally, the chord of the NACA0012 airfoil. The Reynolds number is defined as Re $= U\,c/\nu$, where U is the free stream velocity and ν the kinematic viscosity of the considered fluid.

Table 1 reports some details of the five geometries studied in the present work. The third column indicates the spatial resolution adopted in the RPD domain closest to the body. the highest spatial resolution $c/\Delta r_1$, where Δr_1 is the mean distance of the points belonging to the RPD, is used in this domain in order to accurately resolve the boundary layers. A resolution of $c/\Delta r_1 = 1250$ is adopted for the flat plate, the triangle and the square, in order to accurately resolve the flow near the corners. A lower resolution $c/\Delta r_1 = 800$ is used for the circle because of its smooth shape.

The resolution used to simulate the NACA0012 airfoil is the highest among all the bodies presented in this work $c/\Delta r_1 = 1600$. Such a high resolutio is needed for an accurate description of the flow field around the trailing edge (see also Durante et al. (2020)).

The fourth column of table 1 reports the simulations end time. Different t_{end} are adopted according to the time behaviours of the drag and lift forces. For example a longer simulation time has been considered for the circular section with respect to the other geometries. In this case the forces spectrum is is characterized by lower frequencies which needs longer times to be correctly captured. Finally, the number of domains used is shown in the last column. It is interesting to note that, while for the first three geometries $N_{domin} = 10$, a different number of domains has been considered for the circle and the airfoil. The reason of this choice is the use of different t_{end} which leads to a different wake length (*i.e.* longer for the circle and shorter for the NACA) with respect to the other test-cases.

A free stream with constant intensity U along the x-axis is considered in all the simulations. In order to avoid an impulsive start, the final value of U is reached through an acceleration ramp described by:

$$u_\infty(t) = \begin{cases} \dfrac{U}{2}\left[1 - \cos\left(\dfrac{\pi t}{t_r}\right)\right] & t \le t_r \\ U & t > t_r \end{cases} \qquad \text{and} \qquad a_\infty(t) = \begin{cases} \dfrac{U\pi}{2t_r}\sin\left(\dfrac{\pi t}{t_r}\right) & t \le t_r \\ 0 & t > t_r \end{cases} \tag{21}$$

N	Geometry	$c/\Delta r_1$	$t_{end}U/c$	N_{domain}
1	Transverse flat plate	1250	100	10
2	Equilateral triangle	1250	100	10
3	Square	1250	100	10
4	Circle	800	300	15
5	NACA0012	1600	80	8

Table 1: List of the different geometries considered. The third column is the highest spatial resolution $c/\Delta r_1$ adopted close to the body (first domain), where Δr_1 is the mean distance between the vortices within the first domain. The fourth column is the dimensionless final time of the simulation. The fifth column reports the number of domains adopted.

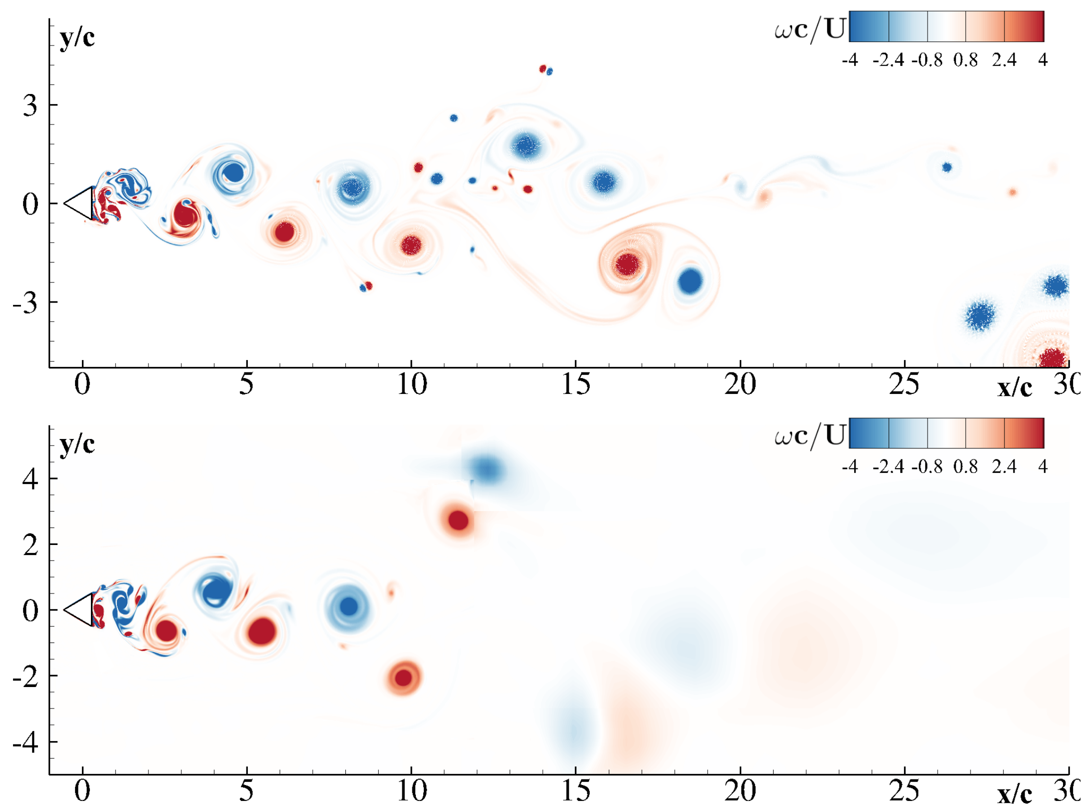

Figure 7: Sketch of the vorticity far field for the flow past a triangular cylinder at Re=10,000 with the DVH (**top**) and FVM (**bottom**) at the final simulation time. For $x > 10c$ the coarsening of the FVM mesh induces an evident numerical dissipation that makes the comparison between the solutions meaningless in this region.

where $t_r = c/U$ and a_∞ is the free stream acceleration.

The results obtained using the DVH method are compared with the ones of the FVM code described in section 4 in which the same velocity ramp has been adopted. The comparisons are made in terms of vorticity field, lift C_l and drag C_d coefficients as well as of pitching moment C_m. The force coefficients are defined as:

$$C_d = \frac{F_x}{1/2\rho\, U^2\, c}\,, \qquad C_l = \frac{F_y}{1/2\rho\, U^2\, c}\,, \qquad C_m = \frac{M_z}{1/2\rho\, U^2\, c^2} \tag{22}$$

where ρ is the fluid density, F_x and F_y are the force components acting on the body along the x and y directions. The pitching moment M_z refers to the origin of the reference frame, which always coincides with the geometric center of the body.

The comparison between FVM and DVH in terms of vorticity field is reasonable up to 10 characteristic lengths from the body. As highlighted in figure 6, a refinement block past the body was designed for the FVM code in order to guarantee that the resolution is fine enough for the wake description. After that block, as clarified in figure 7, the coarsening of the structured mesh causes a rapid dissipation of the vortex structures, thus making the comparison meaningless.

5.1. Computational resources

All the DVH and FVM simulations have been performed on four workstations equipped with eighteen cores Intel® Xeon® Gold 6128 CPU @ 3.40GHz.

For the DVH an OpenMP parallelization was implemented, the maximum number of particles used is of order 10^6 for all the simulations with an allocated memory not exceeding 1 Gbyte. The efficiency η, defined as:

$$\eta \;=\; (\text{Total CPU time} \times N^\circ_{\text{cores}})\,/\,(N^\circ_{\text{iterations}} \times N^\circ_{\text{vortices}})$$

is about 100μs for the DVH solver. Although the in-house developed DVH code may be further optimized, its efficiency is aligned with other vortex particle solvers mainly because of the Fast Multipole Method used for the solution of the Poisson equation (see *e.g.* Rossinelli et al. (2015)).

For the FVM solver, the efficiency η is referred to the number of cells:

$$\eta \;=\; (\text{Total CPU time} \times N^\circ_{\text{cores}})\,/\,(N^\circ_{\text{iterations}} \times N^\circ_{\text{cells}})$$

and it turns to be about 65μs. The multi block domain decomposition of the FVM mesh grid allows a more efficient MPI parallelization, which ensures a high scalability up to hundreds of cores and is nearly linear on the 18 cores considered here.

The CPU time of the test-cases discussed, together with some major parameters, are reported in table 2 for both solvers.

It is worth to underline that the design of the multiple domains is rather similar for the firsts three geometries, namely the flat plate, the triangle and the square. An analogous blocks design was adopted in Xnavis. It is interesting to note that the number of vortices N_{max} generated for the flat plate is significantly higher than the triangle and the square, even if the same spatial resolution $c/\Delta r_1$ was adopted. The reason behind this relies on the particular development and arrangement of the wake. As shown in figure 11, the transverse flat plate produces big and intense dipole structures that delay the crossing of a vortex particle to a coarser domain. The particles remain confined in the same high resolution domain by the upward current generated by the dipole for a significant simulation time and thus, the total number of vortex particles keeps growing due to the diffusion step.

Regarding the Xnavis numerical domain, the resolution close to the body surface is similar to the one adopted with the DVH, although in the body fitted blocks a stretching must be used to match, as far as possible, the near body mesh with the wake one, thus avoiding a discontinuity in the spatial resolution between chimera cells. Xnavis numerical domains were designed without considering any specific wake peculiarity, depending only on the body complexity and some heuristic considerations. For this reason, the number Xnavis cells is rather smaller when compared to the number of vortices adopted in the DVH for the flat plate while it is generally greater in the other cases.

The simulations of the flow past a NACA0012 airfoil at varying angle of attack are directly compared with data available in literature using a different mesh-based solver.

Beside the above considerations, when comparing the CPU costs of the DVH and of a FVM solver, the following aspects need to be pointed out:

- DVH uses a vorticity while the FVM a velocity-pressure formulation of the Navier-Stokes equation, meaning that the FVM will compute the vorticity field with a lower degree of accuracy.

- A vortex particle scheme is self-adaptive, because the vorticity formulation allows to discretize only the rotational flow regions. Conversely, in the FVM the mesh must be *ad hoc* designed, with an *a priori* estimation of high velocity gradients areas.

	DVH			Xnavis (FVM)		
N	N_{max} Vortices	$N_{iterations}$	CPU time (18 cores)	N_{cells}	$N_{iterations}$	CPU time (18 cores)
1	5,200,000	62,500	29 days	1,530,000	100,000	8 days
2	2,400,000	62,500	11 days	2,260,000	100,000	10 days
3	1,607,000	62,500	13 days	2,940,000	100,000	12 days
4	1,895,000	60,000	9 days	2,260,000	300,000	28 days
5	2,710,000	64,000	16 days	–	–	–

Table 2: Comparison between DVH and FVM numerical costs.

- In DVH the far-field conditions are automatically satisfied (see *e.g.* Giannopoulou et al. (2019)), whereas in FVM a wide background block with a significant mesh stretching must be introduced, in order to make the domain frontiers effects negligible.

- The spatial resolution of the finite volume meshes needs to be coarsened to limit the total number of cells and avoid velocity gradients near the domain boundaries (which would imply spurious reflections of the solution and numerical instabilities).

- The spatial distribution of FVM numerical cells can be easily controlled by means of mesh stretching. Therefore it is possible to significantly increase the spatial resolution inside the boundary layers. In all the simulations presented in this work, similar resolutions in the body fitted regions have been used for the two solvers.

- Finally, FVM requires a non-negligible cost in terms of human work for grid design and the pre-processing, which may become critically long while increasing grid complexity.

5.2. Flow past a transverse flat plate

A flat plate of length c is oriented transversely with respect to the incoming flow. During the transient stage, the shear layer detaches from the flat plate edges becoming unstable already at the beginning of the simulation breaking into small vortices. This instability, however, does not prevent the formation of two recirculation zones behind the flat plate. As shown in figure 8-a, the small vortices generated by the shear layer instability form a larger symmetric dipole structure which grows with time in the stable configuration shown in figure 8-b. In figure 8-c, the symmetry of the vortex dipole is broken so that the shedding mechanism starts just afterwards, as shown in figure 8-d. From this plot it is possible to observe that the shear layer detaching from the upper edge is not stable anymore and a fragmentation in small vortex patches occurs. The shedding mechanism characterized by the formation of a wider vortex patch surrounded by little dipoles may be here recognized in figures 8-e and 8-f. The same phenomenon was also found numerically in Durante et al. (2020) for the flow past an inclined thin ellipse and experimentally in Pierce (1961) for different geometries.

It is important to highlight that the peculiar arrangement of the small dipoles during the shedding is a specific characteristic of $Re = 10,000$, so that the capabilities of a solver in reproducing these complex kind of vorticity patterns can be benchmarked with such kind of simulations.

In order to show how challenging these kind of simulations can be, a comparison between the results obtained using the DVH solver and the FVM is shown in figure 9.

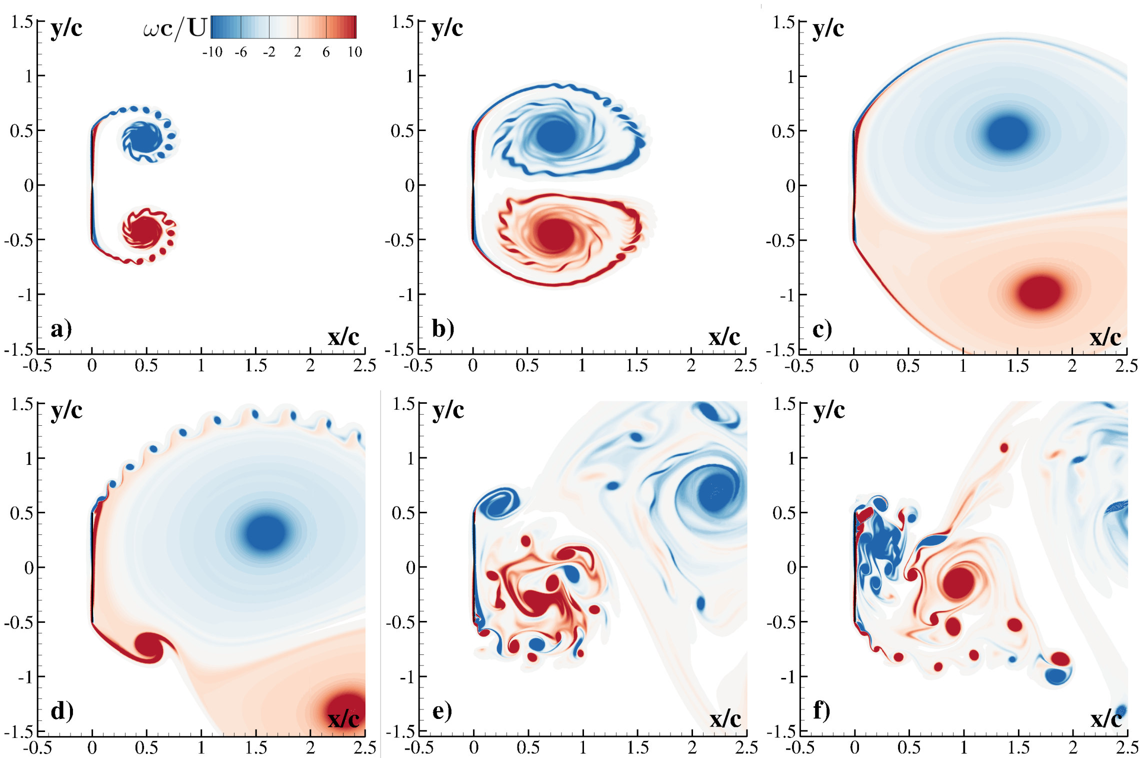

Figure 8: Flow past a transverse flat plate at Re=10,000. From **up-left** to **bottom-right** the time evolution of the vorticity wake field. The related time instants are: **a**: tU/c=2.25, **b**: tU/c=4.75, **c**: tU/c=30.00, **d**: tU/c=34.75, **e**: tU/c=49.75, **f**: tU/c=74.75.

Both DVH and FVM capture the main flow features, but the richness in terms of vortex scales observed in the DVH solution (left frame of figure 9) is not appreciable in the corresponding FVM one (right frame of figure 9).

As stated in section 5 and shown in figure 7, the vorticity fields obtained with both algorithms can be compared (at most) up to a distance of about ten characteristic lengths from the body, *i.e.* $x < 10$c, where the FVM numerical dissipation is still limited. In this case, however, the structured mesh of the FVM solver suffers from a significant numerical viscosity even near the body, as shown in figure 9, although the body fitted grid resolution is comparable with the DVH.

In figure 10 the lift and drag coefficients time histories are represented. In these plots a long transient is visible, corresponding to frames a, b and c of figure 8, lasting up to $tU/c \simeq 34.75$. The drag coefficient fast growth that can be appreciated at the beginning of the simulation is caused by the acceleration ramp used to avoid an impulsive start: the free stream acceleration,in fact, generates an added mass effect which increases the drag

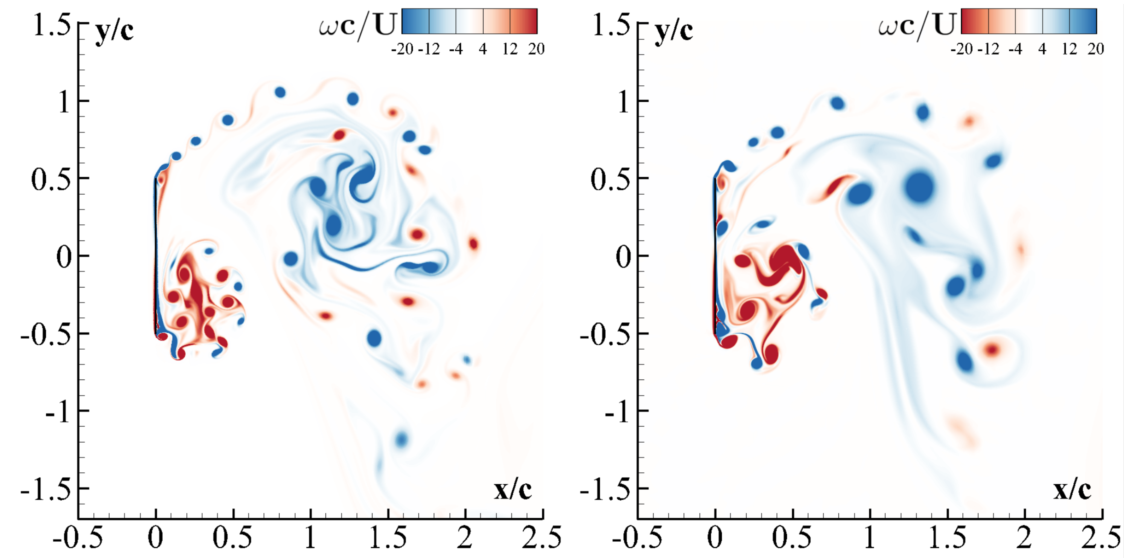

Figure 9: Flow past a transverse flat plate at Re=10,000. Comparison between DVH (**left**) and FVM (**right**) vorticity fields.

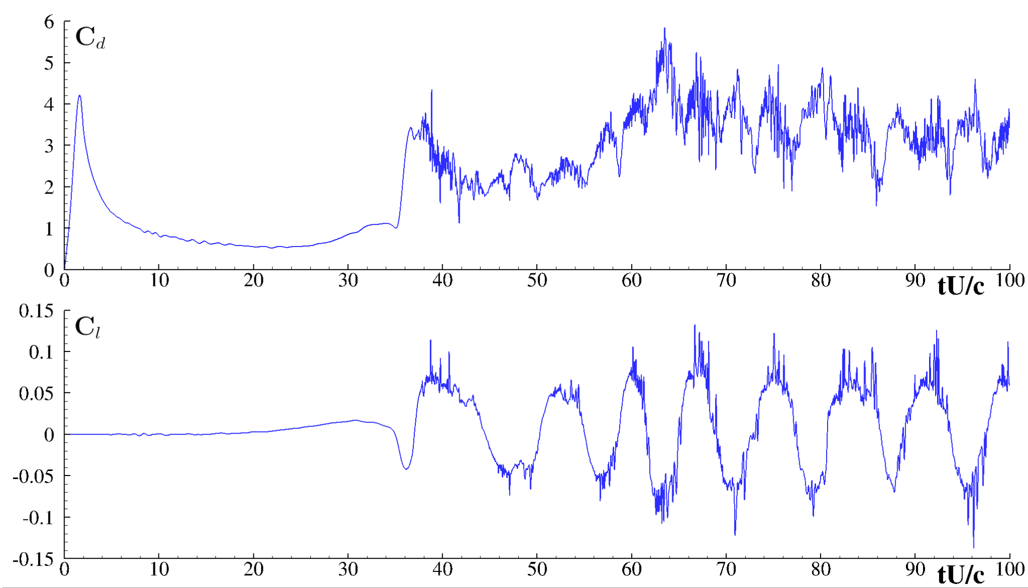

Figure 10: Flow past a transverse flat plate at Re=10,000. Drag (**top**) and Lift coefficients (**bottom**) from DVH simulations.

522 coefficient. At the same time the lift coefficient remains close to zero. Afterwards, while

the recirculation zones widen, the drag coefficient C_d lowers up to its minimum value around $C_d = 0.5$. When the shedding begins, the drag increases again and start to oscillate rapidly and irregularly with small amplitudes, as shown in top plot of figure 10. Two different behaviors can be appreciated when looking at C_l time history (bottom plot of figure 10): large amplitude and low frequency oscillations are superimposed with small fast ones.

The fast oscillations appearing in drag and lift coefficients can be better appreciated in top frames of figure 11, where the magnifications of the C_d and C_l time histories are shown. These oscillations are caused by the fragmentation of the shear layer into small vortices

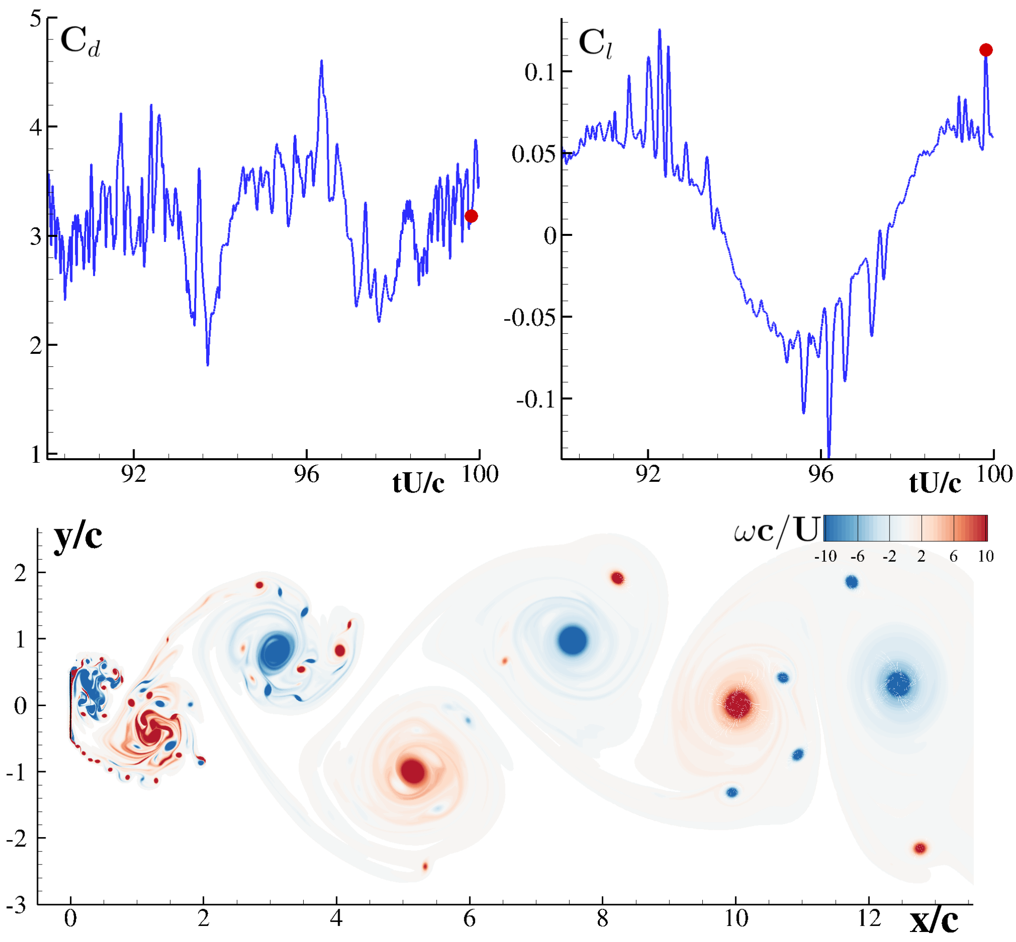

Figure 11: Flow past a transverse flat plate at Re=10,000 and $tU/c = 99.81$. The vorticity wake field on **bottom**. On **top** the drag (left) and lift (right) signals with a red dot corresponding to the shown time instant.

observed during the shedding which, in turns, locally induces fast velocity fluctuations. In bottom plot of figure 11 the vorticity field at the end of simulation is depicted. The far field, constituted mainly by large vorticity structures generated by the merging of the small vortices, can be appreciated. The multi-resolution algorithm adopted in the present work shows a remarkable ability in maintaining also smaller vorticity patches at 10 - 12 lengths from the plate, *i.e.* $x = 10c - 12c$.

In table 3 the mean drag C_d, lift C_l and pitching moments C_m, evaluated for $tU/c > 60$ are reported together with their standard deviations. In order to highlight the ability of the DVH body fitted approach in accurately reproducing the forces acting on the body, the results are compared with those obtained with the FVM method, showing a good agreement. The mean values for C_l and C_m have not been reported, being them close to zero as expected.

	C_d	C_l	C_m
DVH	3.50 ± 0.65	± 0.054	± 0.378
FVM	3.46 ± 0.50	± 0.067	± 0.386

Table 3: Flow past a transverse flat plate: comparisons of means and standard deviations of forces and torque times signals for DVH and FVM codes.

5.3. Flow past a triangular cylinder at Re=10,000.

The flow past an equilateral triangular cylinder (with side c) at $\mathrm{Re} = 10,000$ is here analysed. The triangle is oriented with the height aligned with the free stream and the corresponding vertex pointing in the opposite direction, as shown in figure 12.

The simulations carried out with both solvers are compared in figure 12, where the vorticity fields are reported at time instants with similar wake development. As already seen in section 5.2 for the flat plate, the shear layers detaching from the sides of the triangle during the transient form a large dipole behind the body, as shown in left column of figure 12. It is worth noting that for the FVM the dipole is rather stable during its growing, whereas for the DVH the clockwise and anticlockwise recirculating areas are characterized by an evident oscillatory behaviour (left top frame of figure 12). The reason behind this discrepancy relies on the numerical strategies used for simulating the vorticity dynamics: with the DVH the RPD close to the body is not symmetric with respect the x-axis. Conversely, the FVM uses a structured grid that matches the symmetry of the body.

This also implies that the solutions obtained with a Finite Volume Method are generally “stable” for longer times and the shedding inception is usually delayed when compared with the DVH solutions.

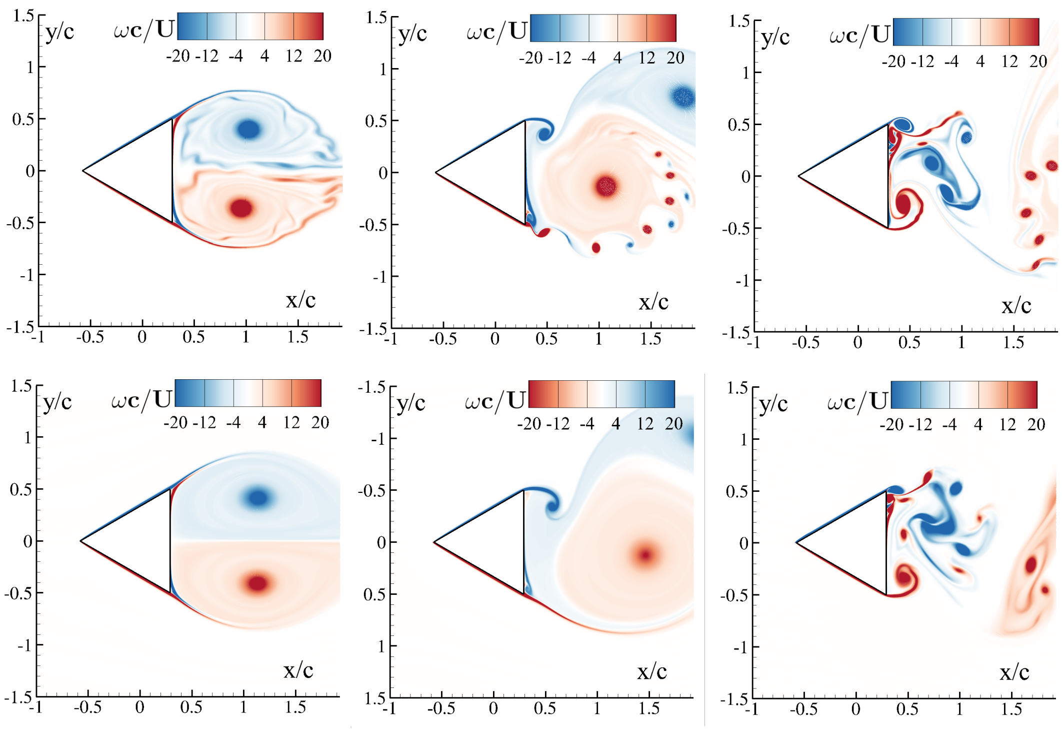

Figure 12: Simulation of the initial stages of the flow past a circular cylinder at Re=10,000. On **top** row the DVH simulation while on **bottom** row the FVM one. From **left** to **right**, the non-dimensional times tU/c sketched are: 6, 10.3 and 12.9 for DVH and 10.8, 30 and 34.1 for FVM.

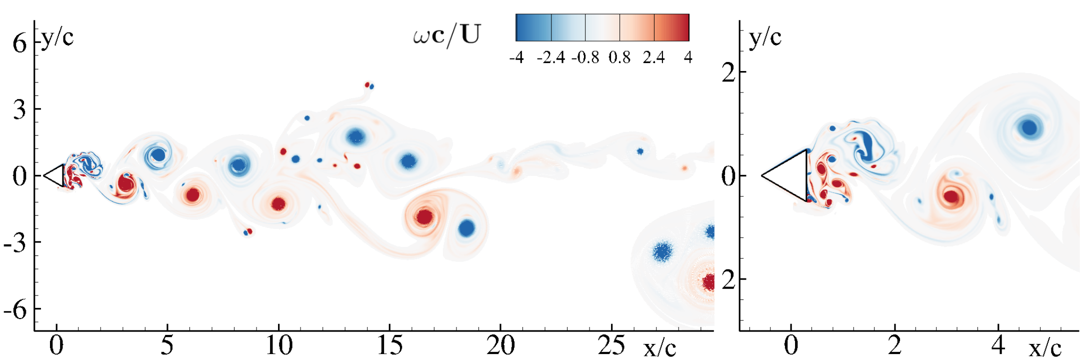

Figure 13: Vorticity far field for the flow past a circular cylinder at Re=10,000 at tU/c=100.

This difference is also visible from the force time histories in figure 14, where the transients related to the dipole formation and growth are longer for the FVM than for the DVH. Specifically, the transient for FVM is about three times longer than for the DVH.

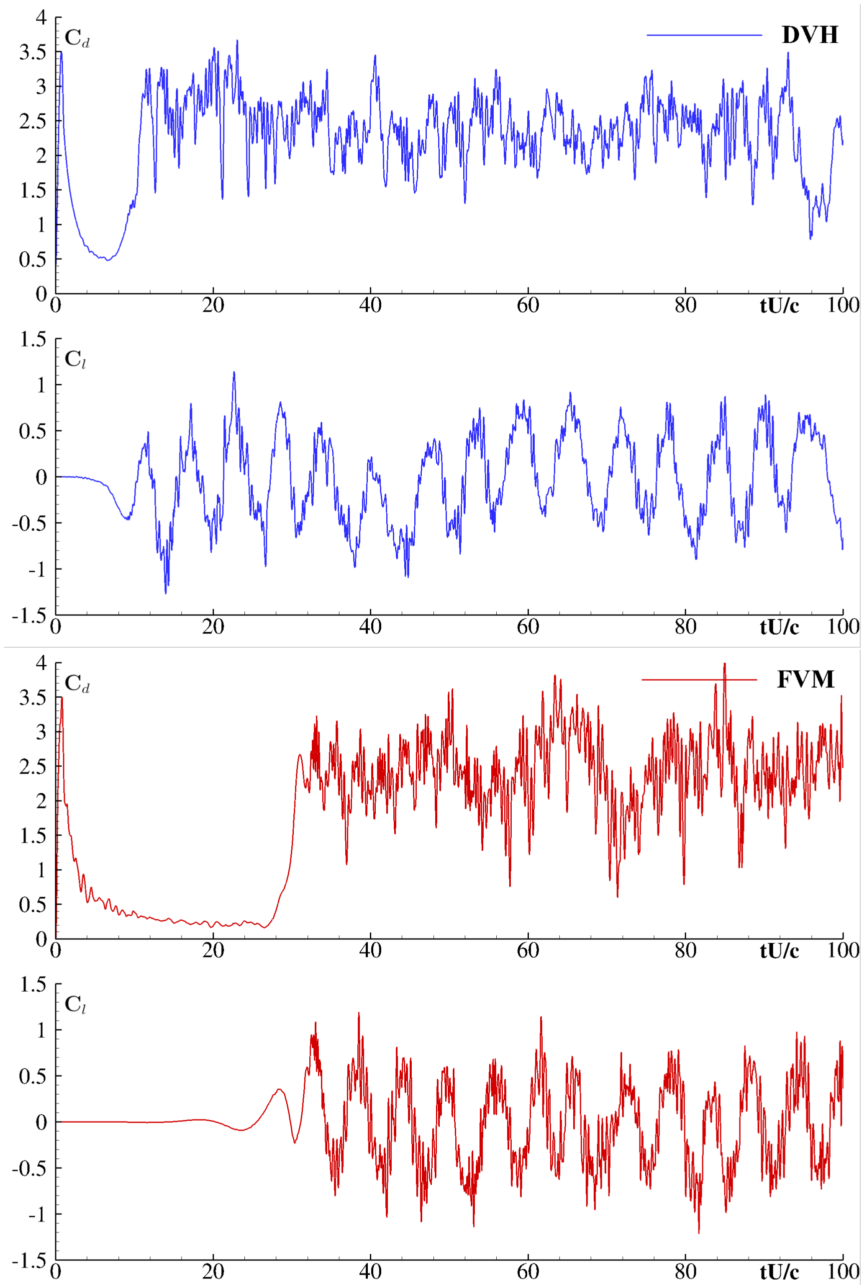

Figure 14: Flow past a triangular cylinder at Re=10,000. Comparison of drag and lift coefficients time histories between DVH (**top**) and FVM (**bottom**) algorithms.

The onset of shedding mechanism is depicted in the center plots of figure 12.

Differences in the shed vorticity between the DVH and the FVM are evident: as previously highlighted, the solution of the FVM shows greater stability in the shear layers detachment, whereas they are fragmented forming little dipoles in the DVH solution.

Besides these differences, the two approaches show a good agreement when comparing the vorticity field for later stages, both being able to capture correctly the same vorticity scales in the near field, as shown in right frames of figure 12.

In figure 13 the DVH vorticity field at $tU/c = 100$ is depicted. The near field is characterized by small scales generated by the shear layer instability, while the far field is dominated by the large dipoles generated by the merging mechanisms typical of planar flows (see *e.g.* Boffetta and Ecke (2012)).

The figure 14 depicts the C_d and C_l time histories for both solvers. Besides the already discussed difences in the transient regime, the two codes show good agreement in evaluating the lift and the drag coefficients, showing a similar shedding frequency. As for the flat plate, also in this case the small oscillations are related to the shear layer instability that, breaking into small vortices, induce a high frequency component in the force signal.

A comparison of C_d, C_l and C_m mean and standard deviation between DVH and FVM is shown in table 4. Because of the symmetry of the problem, the mean values for C_l and C_m are close to zero and, for this reason, are not reported. The time average has been performed without considering the transient regime, $tU/c > 16$ for DVH and $tU/c > 36$ for the FVM respectively and show a fair agreement between the solvers.

	C_d	C_l	C_m
DVH	2.33 ± 0.47	± 0.447	± 0.252
FVM	2.33 ± 0.67	± 0.429	± 0.240

Table 4: Flow past a triangular cylinder: comparisons of means and standard deviations of forces and torque time signals for DVH and FVM codes.

5.4. Flow around a square cylinder at Re=10,000.

In this section the flow past a square cylinder at $\mathrm{Re} = 10,000$ is investigated. The reference length c is the square side.

Figure 15 shows the DVH and FVM vorticity fields developed during the initial stage of the motion. The boundary layers develop over the top and bottom sides. They become unstable close to the left vertices inducing a rolling of the detached vortex structures along the horizontal sides, while the detachment on the right vertices forms two recirculating zones. Looking at the middle and right plots of figure 15, the flow separation rapidly leads to the onset of vortex structures strongly interacting with each other and with the square

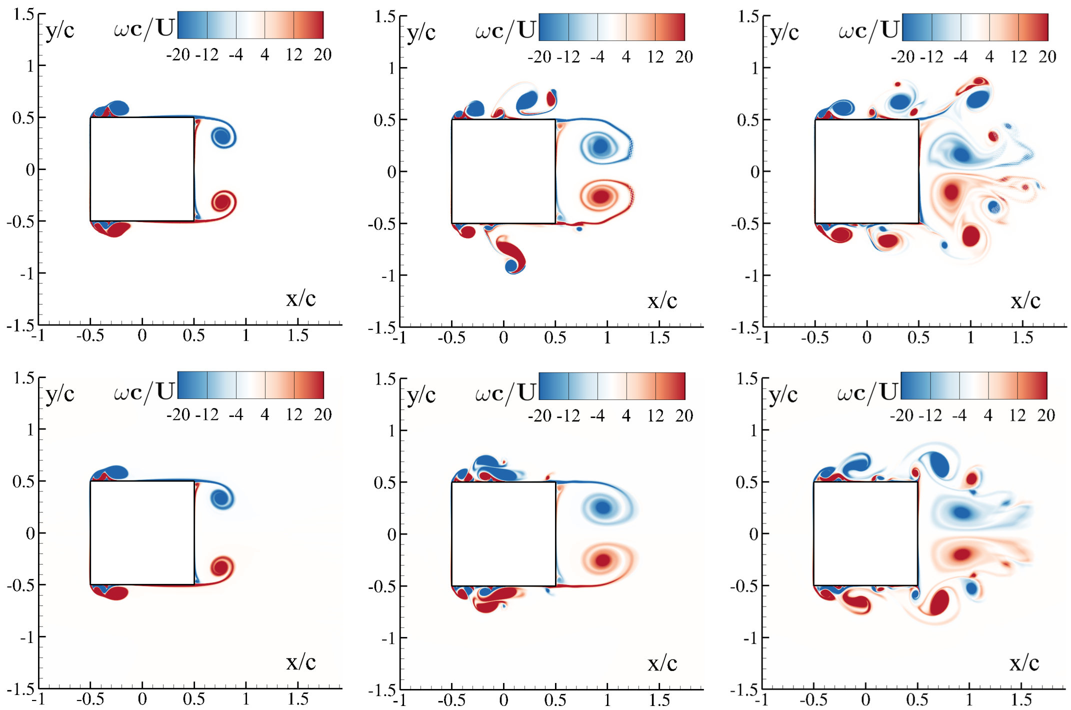

Figure 15: Simulation initial stages of the flow past a square cylinder at Re=10,000. From the **left** to **right**, the non-dimensional times tU/c sketched are: 2, 3 and 4. On **top** row the DVH simulation while on **bottom** the FVM one.

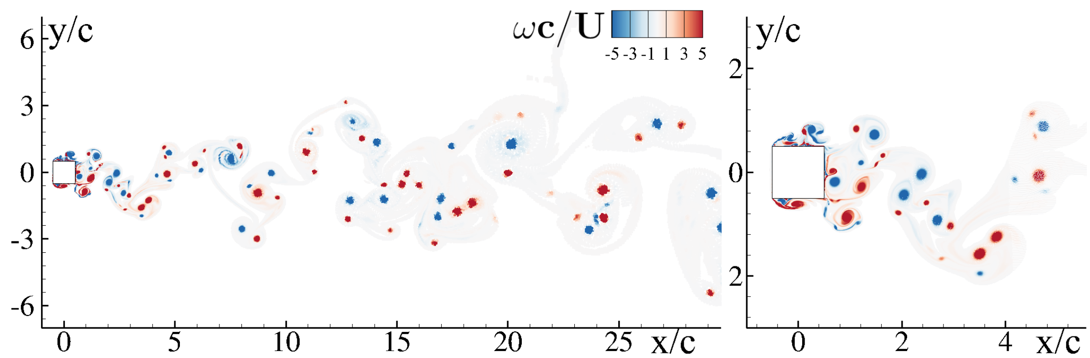

Figure 16: Vorticity far field for the flow past a square cylinder at Re=10,000 at tU/c=75.

sides. The small eddies generated over the top and bottom sides move downstream and directly interact with the recirculating zones, causing the rapid inception of the shedding mechanism.

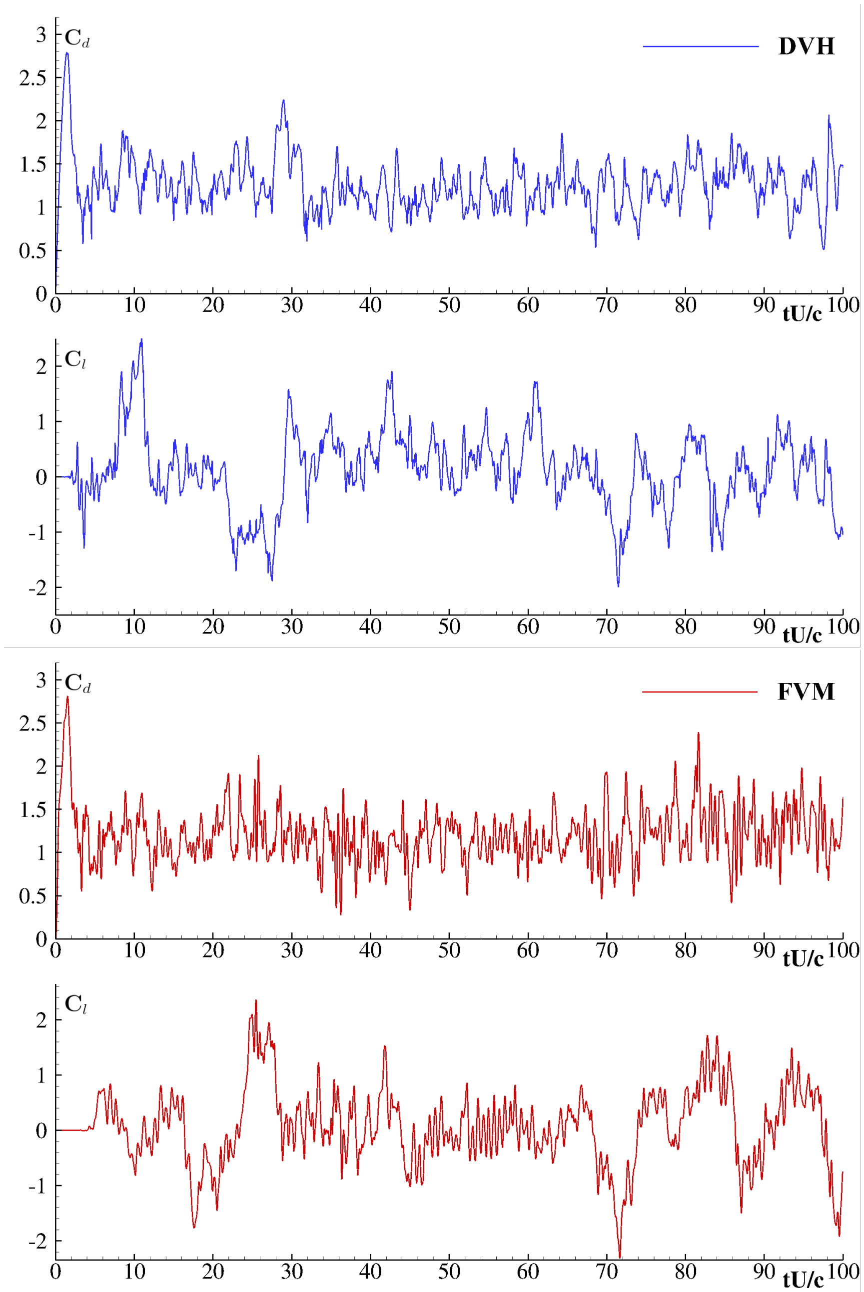

Figure 17: Flow past a square cylinder at Re=10,000. Comparison of drag and lift coefficients time histories between DVH (**top**) and FVM (**bottom**) algorithms.

As previously highlighted, the DVH fields are not symmetric because the adopted RPD iso non-symmetric, as visible on center and right frames of figure 15. Conversely, in the FVM fields the symmetry is strictly preserved during this initial stage of the flow. Beside those differences between DVH and FVM, both the solvers exhibit a very similar transients of the forces as depicted in figure 17.

It is interesting to note that, in this case, the various vortex scales shed in the flow field remain well separated even in the far field. In other words the eddies merging phenomena is less intense and, as a consequence, no main shedding frequency is observed in the lift and drag time histories, as shown in figure 17. The forces evaluated using the two solvers are in good agreement and table 5 reports the comparison of the mean C_d, C_l and C_m together with their standard deviation. The solvers accordance is confirmed on these quantities also. As already commented in sections 5.2 and 5.3, the mean values of C_l and C_m are not reported being close to zero for symmetry reason.

	C_d	C_l	C_m
DVH	1.25 ± 0.26	± 0.687	± 0.131
FVM	1.19 ± 0.29	± 0.717	± 0.118

Table 5: Flow past a square cylinder: comparisons of means and standard deviations of forces and torque time signals for DVH and FVM codes.

5.5. Flow around a circular cylinder at Re=10,000.

In the present section the flow past a circular cylinder of diameter c at $\mathrm{Re} = 10,000$ will be discussed.

As remarked in Durante et al. (2017), in a two dimensional framework and at this Reynolds number the flow remains within the lower sub-critical regime: the shear layers start to fluctuate and only few eddies are formed downstream by their mutual interaction.

As visible in left plot of figure 18, the boundary layers start detaching from the cylinder surface undergoing a roll-up which will generate the two recirculation areas. This dipole arrangement remains stable up to about $tU/c = 10$ for the DVH and about $tU/c = 20$ for the FVM. Afterwards the wake becomes unstable, as visible in top-right plot of figure 18, and the shedding begins.

In figure 18 a comparison of the vorticity fields computed with both solvers is presented. In this case, the shape does not present geometrical singularities so that the vorticity is shed through vortex patches comparable to cylinder size. DVH and FVM solution are in good agreement in terms of vortex scales shed in the flow field.

The figure 19 show the near and far DVH vorticity fields at the end of the simulation. The multi-resolution technique adopted in the DVH is able to follow the small eddies

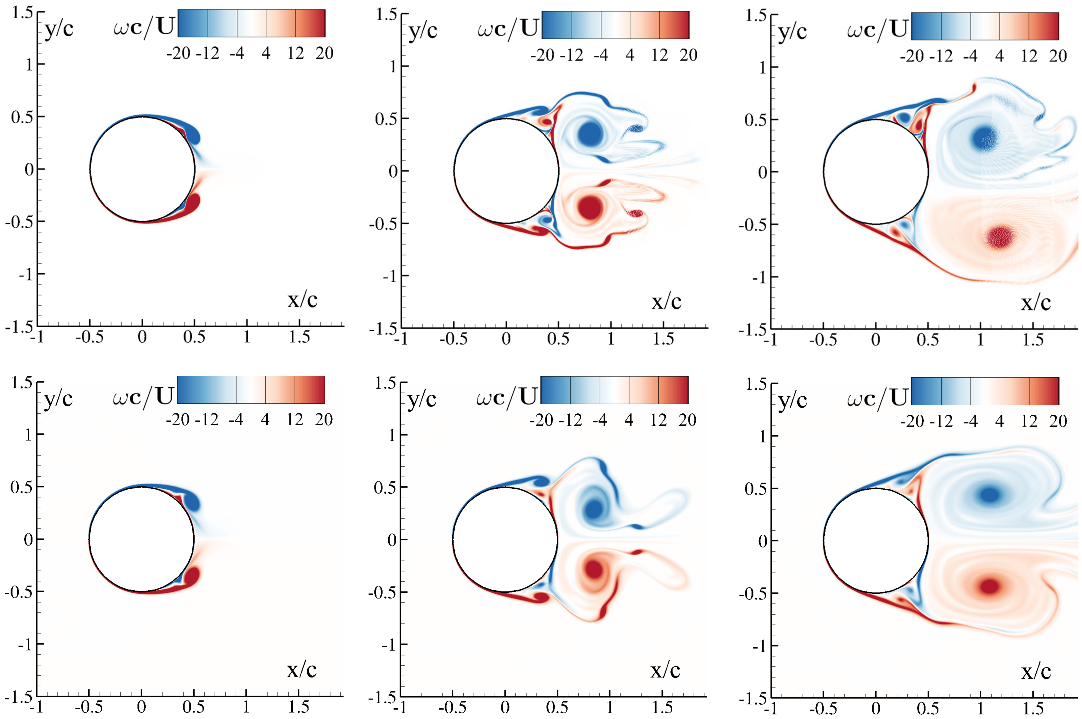

Figure 18: Simulation initial stages of the flow past a circular cylinder at Re=10,000. On **top** row the DVH simulation while on **bottom** row the FVM one are depicted. From **left** to **right**, the non-dimensional times tU/c sketched are: 2, 4 and 12 for DVH and 2.5, 5.2 and 11 for FVM.

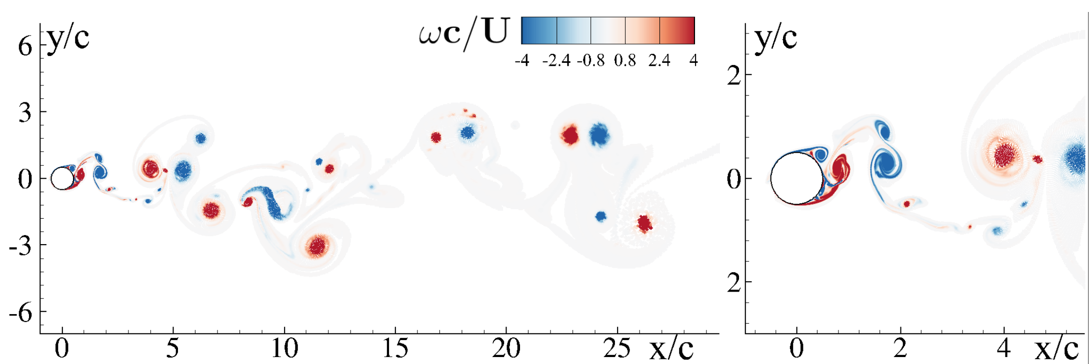

Figure 19: Vorticity far field for the flow past a circular cylinder at Re=10,000 at tU/c=300.

generated by the fragmentation and roll-up of the shear layers and advected toward the far field. The above mechanism leads to an irregular shedding with a rather disordered wake arrangement typical of this Reynolds numbers regime (see also Durante et al. (2021) for

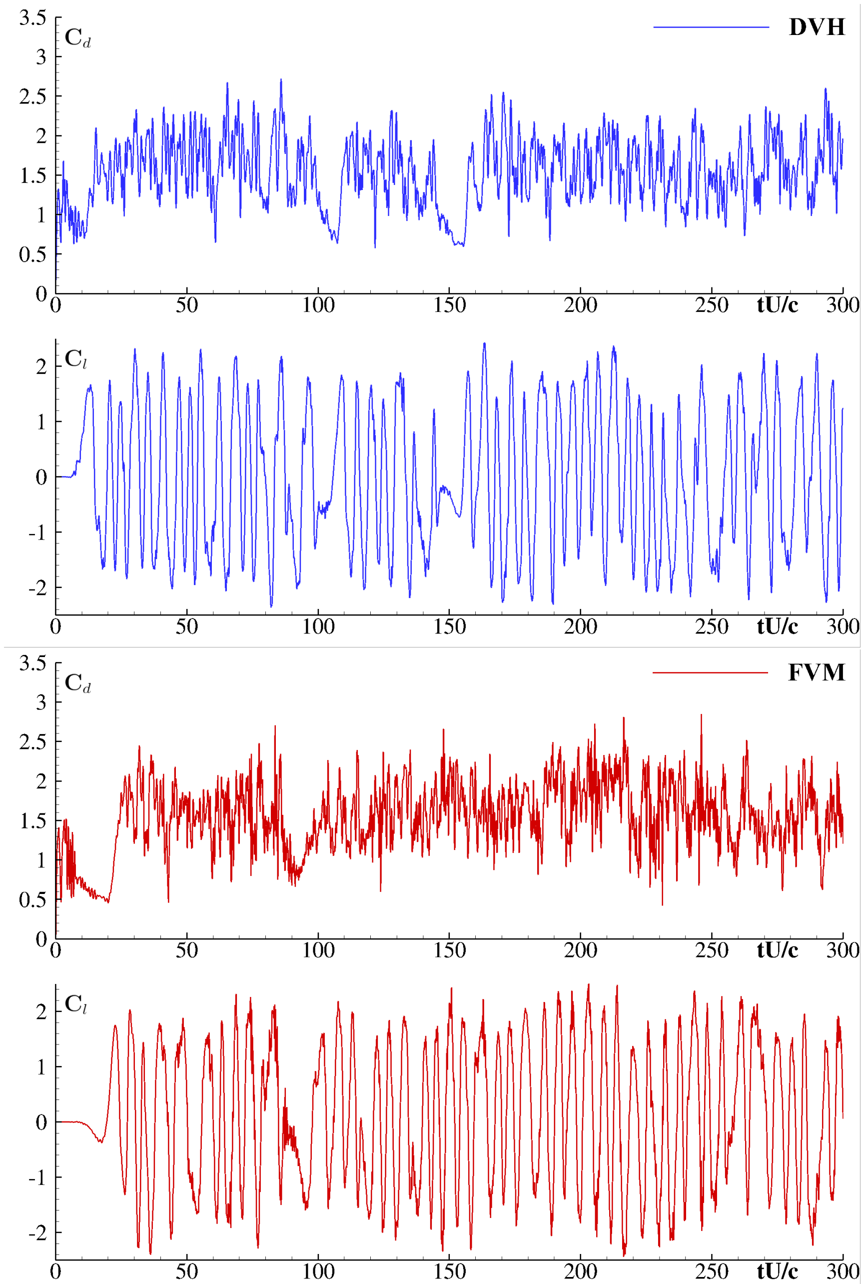

Figure 20: Flow past a circular cylinder at Re=10,000. Comparison of drag and lift coefficients time histories between DVH (**top**) and FVM (**bottom**) algorithms.

an in-depth discussion).

The figure 20 depicts the time histories of the DVH and FVM forces. The comparison between the solvers appears rather encouraging. The lift forces, in particular, exhibit a remarkably similar behaviour with a carrier frequency of $f^* = 0.175 fc/U$ common to both methods (*i.e.* the differences are order 10^{-4}) with the typical features observed and discussed in Durante et al. (2022).

When looking at both DVH and FVM lift time signals it is possible to note that the oscillatory behaviour stops for some cycle. This intermittence is one of the key points discussed in Durante et al. (2022). It is worth noting that this behaviour is correctly reproduced by both solvers, although it requires highly refined meshes near the cylinder surface in order to to be appreciated.

Finally, table 6 reports a comparison between DVH and FVM in terms of mean C_d, C_l and C_m along with their standard deviations. The geometrical regularity of the body makes the outcomes of the two solvers remarkably similar both in terms of average values as well as of their standard deviations. The standard deviations of the pitching moments are very small, as expected for this geometry.

	C_d	C_l	C_m
DVH	1.55 ± 0.43	± 1.261	± 0.002
FVM	1.54 ± 0.43	± 1.257	± 0.002

Table 6: Flow past a circular cylinder: comparisons of means and standard deviations of forces and torque times signals for DVH and FVM codes.

5.6. Flow past an airfoil at varying AoA

In this section the flows past a NACA0012 at varying angle of attack $\alpha = 0°$, $4.5°$, $6°$, $9°$ and $15°$ are discussed. The DVH results are, for these cases, directly compared with the data available in literature. In particular, the numerical works of Sun et al. (2018) and Lee et al. (2015) and the experiments of Ohtake et al. (2007) are taken as reference.

Figure 21 depicts the vorticity fields obtained at the end of the simulation for all the angle of attack analysed. In figure 23 the C_l time histories are shown. As discussed in Durante et al. (2020), for this case the lift time history is more interesting than the drag in order to discuss the wake pattern.

At $\alpha = 0°$ (top plot of figure 21) the top and bottom boundary layers remain attached to the airfoil and only a weak instability is visible in the wake at about 4 chord downstream. This instability is too far from the body to induce an appreciable effect on the lift force. Conversely, for $\alpha = 4.5°$ the vortex shedding is more intense and takes place just on the airfoil trailing edge. The effect of this shedding is visible in the C_l time history (top plot

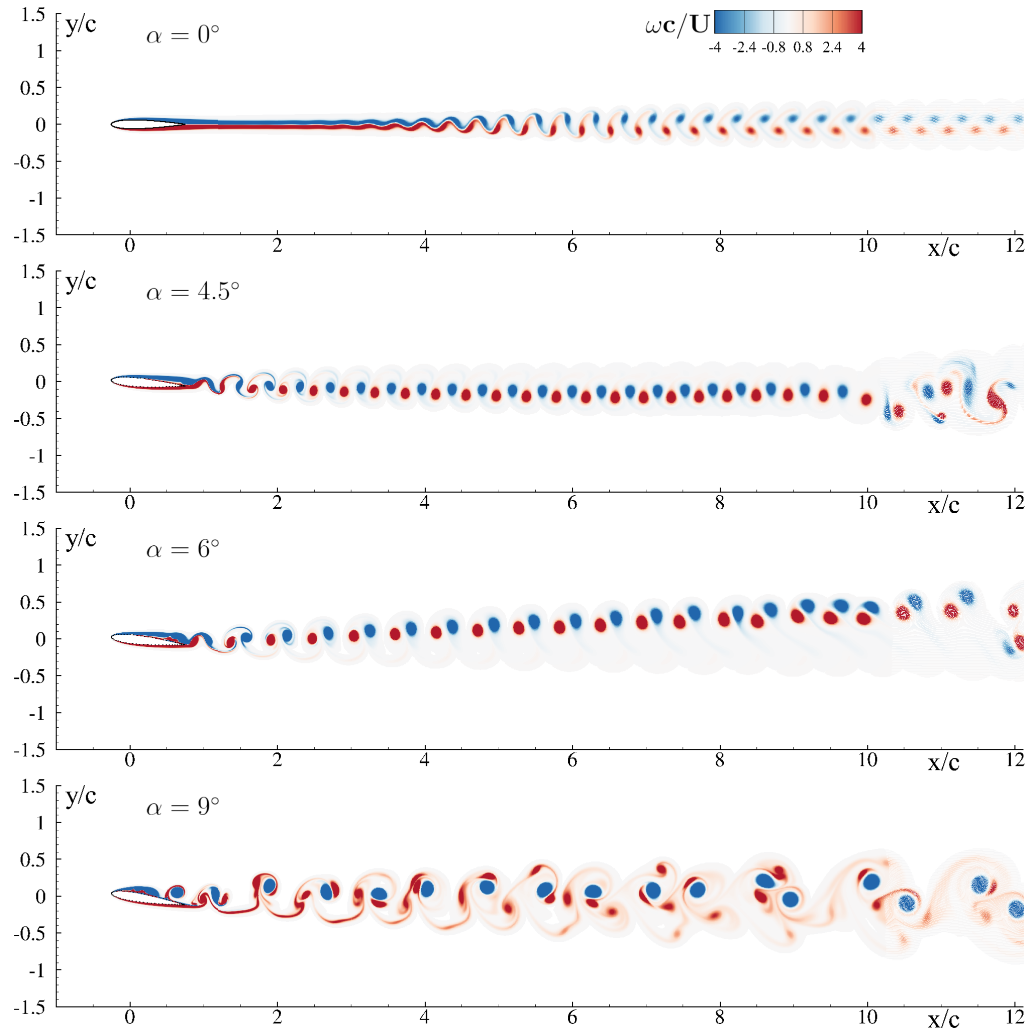

Figure 21: Vorticity far field for the flow past a NACA0012 profile at Re=10,000 and varying angle of attack.

of figure 22) where, after a transient, regular and periodic oscillations produce an ordered dipole arrangement of the wake up 10 chords from the airfoil.

For $\alpha = 6°$ the vortex shedding is characterized by a set of dipoles which, further downstream, bend the wake upward. The periodic shedding of these dipoles has a strong effect also on the C_l time history, where periodic oscillations with large amplitude are established.

At $\alpha = 9°$ the flow separation occurs on the suction side almost in the middle of the foil chord. The separation and following reattachment induce the shedding of dipoles

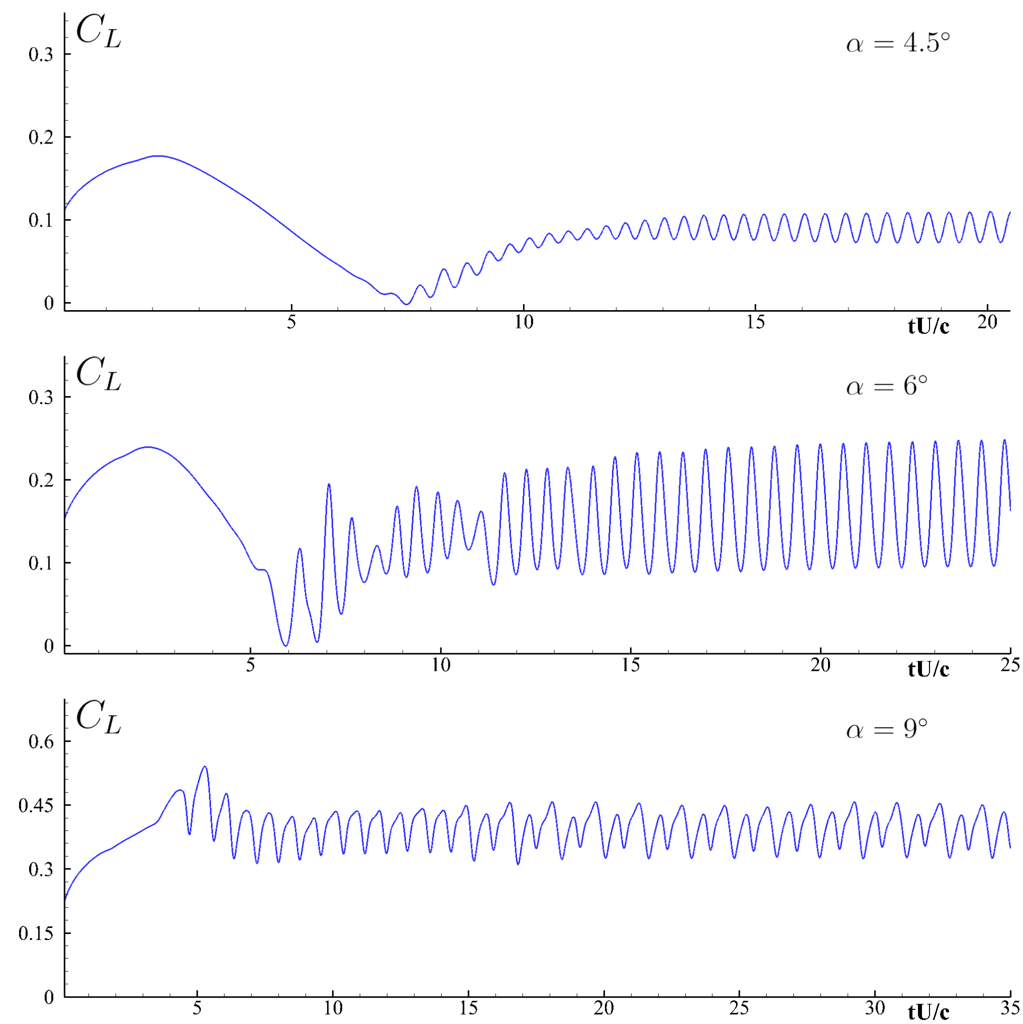

Figure 22: Flow past a NACA0012 airfoil at Re=10,000. Lift coefficients time histories for different angles of attack calculated with DVH algorithm.

characterized by clockwise moment. In this case a filamentation phenomenon can be observed caused by a strong interaction between the shed dipoles. This particular wake pattern has an effect on the C_l time history where a doubling period is observed. These kinds of phenomena are also discussed in Rossi et al. (2018); Durante et al. (2020).

Figure 23 shows the comparison of the mean C_l and C_d computed using the DVH method with the experimental data by Ohtake et al. (2007) and the numerical results by Lee et al. (2015) and by Sun et al. (2018). The DVH results show a fair agreement with

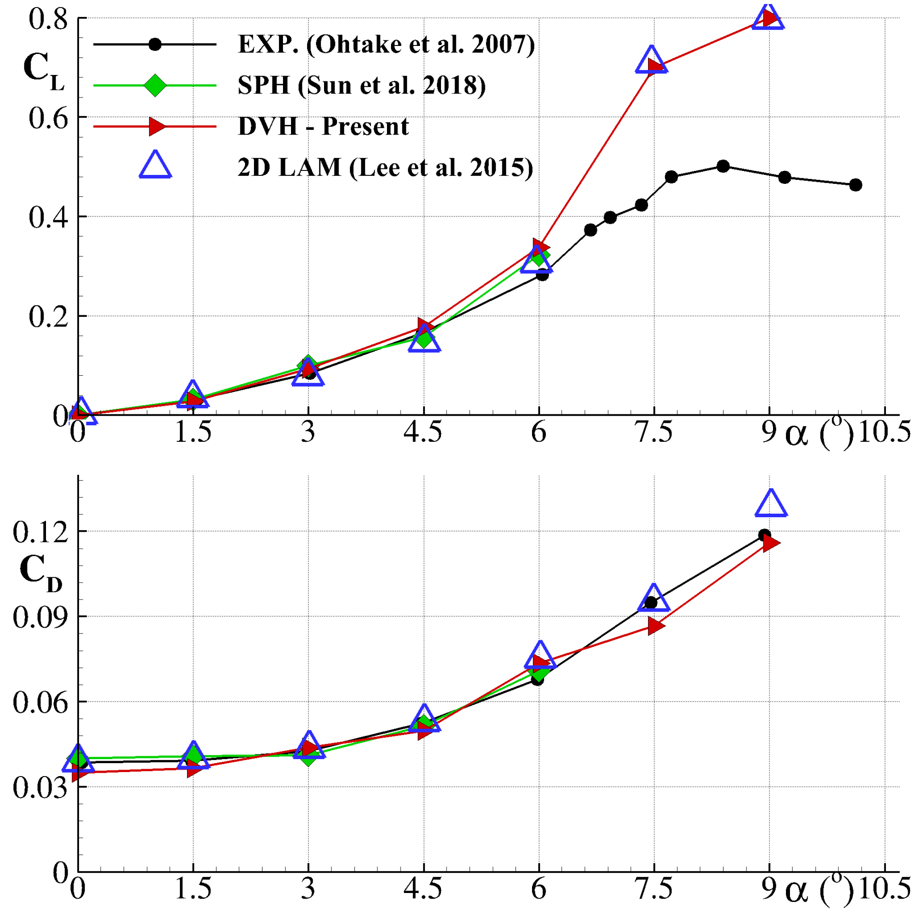

Figure 23: Flow past a NACA0012 airfoil at Re=10,000. Comparison of drag and lift coefficients with the literature, for varying angle of attack

the other numerical results for both the lift and drag coefficients. A comparison with the experimental data, however, is possible only up to an incidence angle of about $\alpha = 6°$: for larger angles of attack the 3D effects dominates the flow generating a smaller lift force.

Finally, in figure 24 the airfoil is pitched at $\alpha = 15°$ and the vortex shedding becomes chaotic with the presence of both large and small vortical structures, as also visible in the lift coefficient time history reported in the bottom plot of the same figure.

6. Conclusions

In the present work a novel multi-resolution algorithm for the Diffused Vortex Hydrodynamics model is introduced. This technique allows to perform long time simulations,

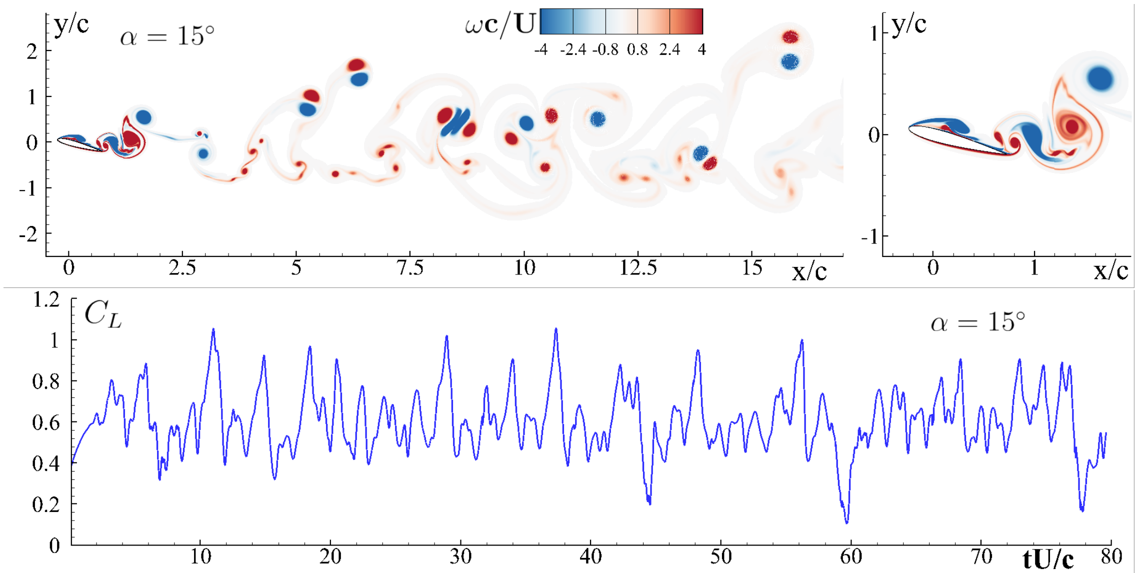

Figure 24: Vorticity far field for the flow past a NACA0012 profile at Re=10,000 and α = 15°.

maintaining the full description of the wake field but significantly limiting the final number of vortex particles used for the simulation. The multi-resolution preserves the total circulation and takes advantage of the Benson algorithm to regularize the particle spatial arrangement during the diffusion step.

The present algorithm is based on the use of synchronized diffusive and advective time steps. Furthermore, sub-domain extensions are adopted with the aim of performing the diffusion step without the mixing of different spatial resolutions. The procedure guarantees the same accuracy of the diffusion process even close to the sub-domain boundaries.

Five distinct benchmark test cases are considered for the validation of the proposed algorithm. Specifically, the viscous flow past a body at Reynolds number equal to 10,000 is studied for five different geometries. The analysis focuses on the global forces as well as the near and far vorticity fields. A Finite Volumes solver has been used as reference solution. The advantages of the DVH formulation with multi-resolution algorithm are highlighted with respect to the standard mesh-based solvers in terms of CPU costs as well as of computational efficiency.

Acknowledgements

The research activity has been developed within the Project Area Applied Mathematics of the Department of Engineering, ICT and Technology for Energy and Transport (DIITET) of the Italian National Research Council (CNR).

AppendixA. Single Vs Multi resolution

In the present appendix we highlight how the multi-resolution algorithm affects the solution of the numerical scheme. The wake fields at the Reynolds number investigated in the former sections (Re=10,000) required from 800 to 1600 vortex particles for unit of length, making unfeasible the use of a single uniform resolution for the whole numerical domain this Reynolds number.

For this reason, we prefer to address a simpler case at Re=1000 with a circular cylinder. For this case the time behaviour of the lift is periodic and, as a consequence, the vortex wake shows a regular arrangement. A single resolution, corresponding to N = 100 vortex

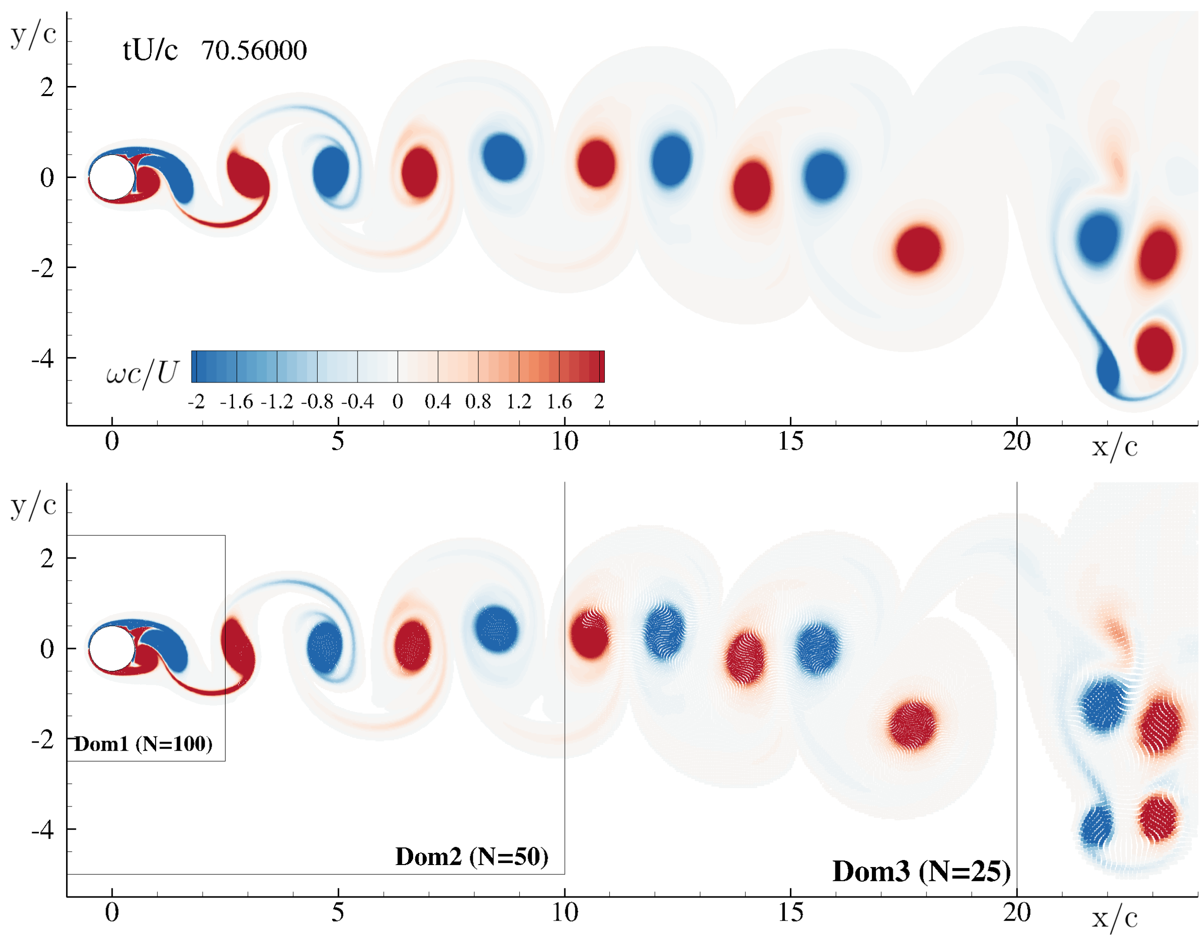

Figure A.25: Flow past a circular cylinder at Re=1000. Single resolution N=100 (**top**) versus multi-resolution (**bottom**) vorticity fields.

particles along the reference length, is compared with a multi-resolution where $N = 100$ is adopted for the body fitted domain only.

In figure A.25 the wake field is depicted in terms of vorticity. The frames show flow fields obtained with uniform resolution versus a multi-resolution. As visible, the dipoles arrangement is very similar also for $x/c > 20$, where the interaction is stronger.

Lift force signal for both uniform and multi-resolution cases are shown in the top frame of figure A.26. During the transient the signals coming from uniform and multi-resolution are superimposed, while small discrepancies appear when the wake looses its symmetry, *i.e.* $tU/c > 28$.

The lift L and the drag D forces on the body are directly calculated from the vorticity

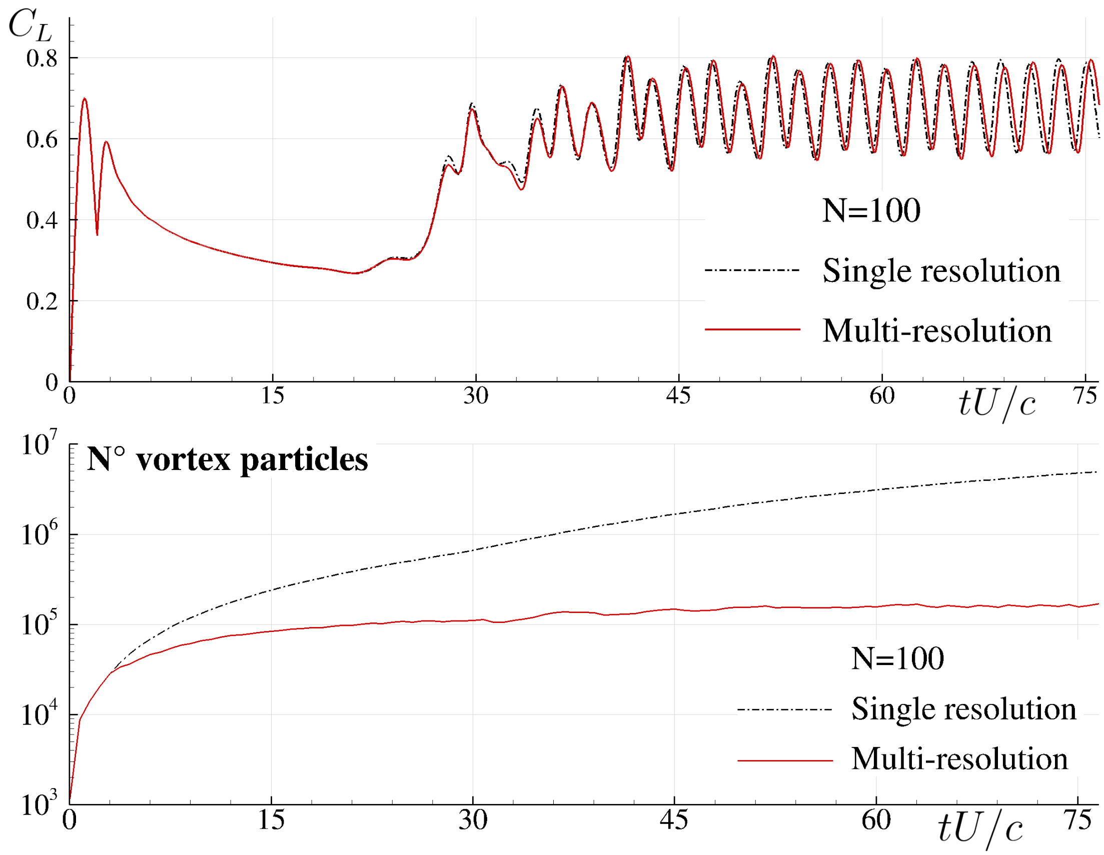

Figure A.26: Flow past a circular cylinder at Re=1000. Single versus multi resolution lift coefficient at $N = 100$ on **top** frame. Number of vortex particles within the numerical domain during the time evolution on **bottom** frame: single versus multi resolution.

field as (see Riccardi and Durante (2007) and Durante et al. (2021)):

$$L = \rho \, \frac{d}{dt} \left(\sum_{j=1}^{N_v} x_j \, \Gamma_j \right) , \qquad D = \rho \, \frac{d}{dt} \left(\sum_{j=1}^{N_v} y_j \, \Gamma_j \right) \tag{A.1}$$

where x_j and y_j are horizontal and vertical components of the j-th vortex position. This means that the agreement between single and multi resolution of the lift time signals denotes that the vorticity distributions share some similarities. In particular, the first moments of the vorticity are well preserved when passing from uniform to multi-resolution. It is worth noting that the DVH scheme, thanks to the vorticity diffusion procedure discussed in section 2, preserves exactly the total circulation, *i.e.* the zero moment of the vorticity (for more details on this topic see Rossi et al. (2015b)).

In the bottom frame of figure A.26, the total number of vortex particles within the numerical domain is reported. It is important to highlight that the total number of vortex particles generated with the uniform resolution is one order of magnitude larger than with the multi-resolution at $tU/c \sim 75$. It may also be appreciated that with a multi-resolution the total number of vortex particles never exceeds 200,000 whereas it rises over 5 millions with a uniform resolution in the time range $tU/c \in [0, 75]$, significantly affecting the DVH capabilities for long-time simulations.

AppendixB. A convergence test using the proposed multi-resolution algorithm

In the present appendix the convergence of the numerical scheme is discussed. As for the AppendixA, we refer the investigation to the flow past a circular cylinder at Re=1000.

The lift force time signal is shown for three different resolutions (*i.e.* N=50, 100, 200) in figure B.27. In order to highlight the different rates of convergence for different time ranges, the transient stage and the periodic regime are reported in two separate frames. From both plots it may be appreciated a clear superposition between medium (N=100) and fine (N=200) resolutions, whereas the differences with the coarse resolution (N=50) are more evident.

In order to quantify those differences a convergence order is estimated for $tU/c \in [0, 25]$ and $tU/c \in [82, 102]$. The convergence rate for the lift force is measured in terms of L_1 norm:

$$\varepsilon_{12} = \int_{t_0}^{t_1} \left| L^{(2)} - L^{(1)} \right| dt \tag{B.1}$$

where $L^{(1)}$ is the lift value computed at the finest resolution, N=200, and $L^{(2)}$ the value computed with a particle distribution for which N is halved, N=100. In order to obtain a convergence rate, a coarser resolution with N halved again, N=50, is used and the computed value of the lift force is indicated with $L^{(3)}$.

The convergence rate is then given by:

$$C(L) = \frac{\log(\varepsilon_{12}/\varepsilon_{23})}{\log 2}\,. \tag{B.2}$$

In the periodic regime (right frame of figure B.27) the convergence rate is about 2 while in the transient time range (left frame of figure B.27) rises up to 3.8.

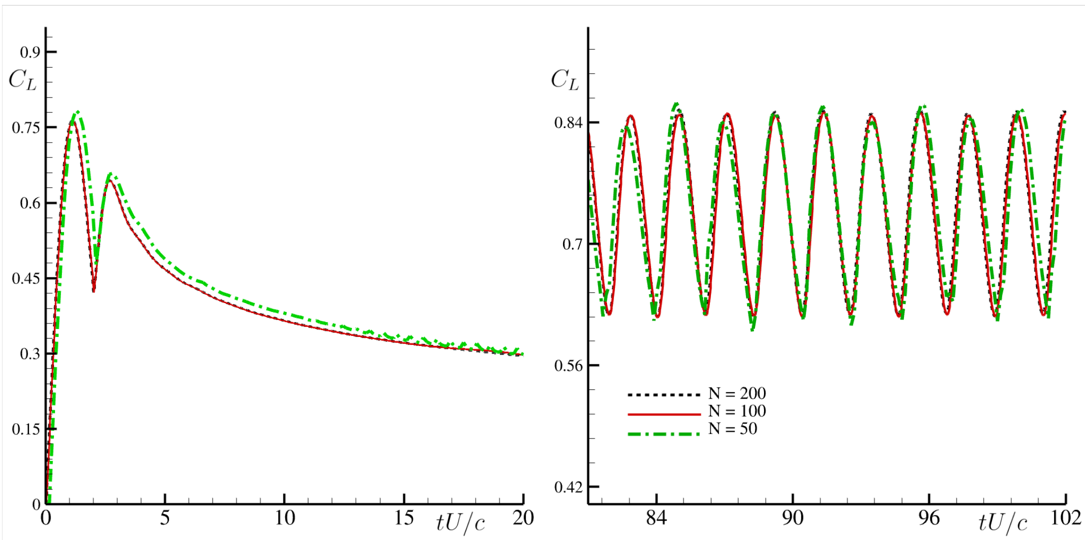

Figure B.27: Flow past a circular cylinder at Re=1000. Lift coefficients convergence in terms of the time signals for three resolutions. On the **left** the transient stage, on the **right** the periodic stage.

References

Badrinath, S., Bose, C., Sarkar, S., 2017. Identifying the route to chaos in the flow past a flapping airfoil. European Journal of Mechanics-B/Fluids 66, 38–59.

Barba, L., August 2005. Vortex method with fully meshless implementation for high-Reynolds number flow computations. In: International COnference on High Reynolds Number Vortex Interactions.

Barba, L. A., Leonard, A., Allen, C. B., 2003. Numerical investigations on the accuracy of the vortex method with and without remeshing. AIAA paper 3426.

Benson, M., Bellamy-Knights, P., Gerrard, J., Gladwell, I., 1989. A viscous splitting algorithm applied to low Reynolds number flows round a circular cylinder. Journal of Fluids and Structures 3 (5), 439–479.

Boffetta, G., Ecke, R. E., 2012. Two-dimensional turbulence. Annual review of fluid mechanics 44, 427–451.

Bose, C., Sarkar, S., 2018. Investigating chaotic wake dynamics past a flapping airfoil and the role of vortex interactions behind the chaotic transition. Physics of Fluids 30 (4), 047101.

Broglia, R., Durante, D., 2018. Accurate prediction of complex free surface flow around a high speed craft using a single-phase level set method. Computational Mechanics 62 (3), 421–437.

Broglia, R., Zaghi, S., Muscari, R., Salvadore, F., 2014. Enabling hydrodynamics solver for efficient parallel simulations. In: 2014 International Conference on High Performance Computing Simulation (HPCS). pp. 803–810.

Chorin, A. J., 1973. Numerical study of slightly viscous flow. Journal of Fluid Mechanics 57 (4), 785–796.

Chorin, A. J., 1978. Vortex sheet approximation of boundary layers. Journal of Computational Physics 27 (3), 428–442.

Cohen, A., 2002. Adaptive methods for PDE's: wavelets or mesh refinement? arXiv preprint math/0212414.

Colagrossi, A., Bouscasse, B., Antuono, M., Marrone, S., 2012. Particle packing algorithm for SPH schemes. Computer Physics Communications 183 (8), 1641–1653.

Colagrossi, A., Nikolov, G., Durante, D., Marrone, S., Souto-Iglesias, A., 2019. Viscous flow past a cylinder close to a free surface: Benchmarks with steady, periodic and metastable responses, solved by meshfree and mesh-based schemes. Computers & Fluids 181, 345–363.

Colagrossi, A., Rossi, E., Marrone, S., Le Touzé, D., 2016. Particle Methods for Viscous Flows: Analogies and Differences Between the SPH and DVH Methods. Communications in Computational Physics 20 (3), 660–688.

Das, A., Shukla, R. K., Govardhan, R. N., 2016. Existence of a sharp transition in the peak propulsive efficiency of a low-Re pitching foil. Journal of Fluid Mechanics 800, 307–326.

Di Mascio, A., Broglia, R., Favini, B., 2001. A second order Godunov-type scheme for naval hydrodynamics. In: Godunov Methods. Springer, pp. 253–261.

Durante, D., Giannopoulou, O., Colagrossi, A., 2021. Regimes identification of the viscous flow past an elliptic cylinder for Reynolds number up to 10000. Communications in Nonlinear Science and Numerical Simulation, 105902.

Durante, D., Pilloton, C., Colagrossi, A., 2022. Intermittency patterns in the chaotic transition of the planar flow past a circular cylinder. Physical Review Fluids (Accepted).

Durante, D., Rossi, E., Colagrossi, A., 2020. Bifurcations and chaos transition of the flow over an airfoil at low reynolds number varying the angle of attack. Communications in Nonlinear Science and Numerical Simulation 89, 105285.

Durante, D., Rossi, E., Colagrossi, A., Graziani, G., 2017. Numerical simulations of the transition from laminar to chaotic behaviour of the planar vortex flow past a circular cylinder. Communications in Nonlinear Science and Numerical Simulation 48, 18–38.

Fayed, M., Portaro, R., Gunter, A.-L., Abderrahmane, H. A., Ng, H. D., 2011. Visualization of flow patterns past various objects in two-dimensional flow using soap film. Physics of Fluids 23 (9), 091104.

Giannopoulou, O., Colagrossi, A., Di Mascio, A., Mascia, C., 2019. Chorin's approaches revisited: vortex particle method vs finite volume method. Engineering Analysis with Boundary Elements 106, 371–388.

Graziani, G., Landrini, M., 1999. Application of multipoles expansion technique to two-dimensional nonlinear free-surface flows. Journal of ship research 43 (1), 1–12.

Hannoun, N., Alexiades, V., 2007. Issues in adaptive mesh refinement implementation. Electronic Journal of Differential Equations 15, 141–151.

Hirsch, C., 2007. Numerical computation of internal and external flows: The fundamentals of computational fluid dynamics. Elsevier.

Jia, L., Xiao, Q., Wu, H., Wu, Y., Yin, X., 2015. Response of a flexible filament in a flowing soap film subject to a forced vibration. Physics of Fluids 27 (1), 017101.

Krishnan, H., Agrawal, A., Sharma, A., Sheridan, J., 2016. Near-body vorticity dynamics of a square cylinder subjected to an inline pulsatile free stream flow. Physics of Fluids 28 (9), 093605.

Kurtulus, D. F., 2015. On the unsteady behavior of the flow around NACA0012 airfoil with steady external conditions at Re=1000. International Journal of Micro Air Vehicles 7 (3), 301–326.

Kurtulus, D. F., 2016. On the wake pattern of symmetric airfoils for different incidence angles at Re=1000. International Journal of Micro Air Vehicles 8 (2), 109–139.

Lee, D., Nonomura, T., Oyama, A., Fujii, K., 2015. Comparison of numerical methods evaluating airfoil aerodynamic characteristics at low Reynolds number. Journal of Aircraft 52 (1), 296–306.

Mandujano, F., Málaga, C., 2018. On the forced flow around a rigid flapping foil. Physics of Fluids 30 (6), 061901.

Muscari, R., 2005. Simulation of the flow around complex hull geometries by an overlapping grid approach. In: Proceedings of 5th Osaka Colloquium, Osaka, Japan, 2005.

Muscari, R., Broglia, R., Di Mascio, A., 2006. An overlapping grids approach for moving bodies problems. In: The Sixteenth International Offshore and Polar Engineering Conference. OnePetro.

Ohtake, T., Nakae, Y., Motohashi, T., 2007. Nonlinearity of the aerodynamic characteristics of NACA0012 aerofoil at low Reynolds numbers. Japan Society of Aeronautical Space Sciences 55 (644), 439–445.

Pierce, D., 1961. Photographic evidence of the formation and growth of vorticity behind plates accelerated from rest in still air. Journal of Fluid Mechanics 11 (3), 460–464.

Pulliam, T. H., Vastano, J. A., 1993. Transition to chaos in an open unforced 2d flow. Journal of Computational Physics 105 (1), 133–149.

Reichl, P., Hourigan, K., Thompson, M. C., 2005. Flow past a cylinder close to a free surface. Journal of Fluid Mechanics 533, 269.

Riccardi, G., Durante, D., 2007. Elementi di fluidodinamica: Un'introduzione per l'Ingegneria. Springer Science & Business Media.

Rossi, E., Colagrossi, A., Bouscasse, B., Graziani, G., 2015a. The diffused vortex hydrodynamics method. Communications in Computational Physics 18 (2), 351–379.

Rossi, E., Colagrossi, A., Durante, D., Graziani, G., 2016. Simulating 2D viscous flow around geometries with vertices through the Diffused Vortex Hydrodynamics method. Computer Methods in Applied Mechanics and Engineering 302, 147–169.

Rossi, E., Colagrossi, A., Graziani, G., 2015b. Numerical simulation of 2d-vorticity dynamics using particle methods. Computers & Mathematics with Applications 69 (12), 1484–1503.

Rossi, E., Colagrossi, A., Oger, G., Le Touzé, D., 2018. Multiple bifurcations of the flow over stalled airfoils when changing the Reynolds number. Journal of Fluid Mechanics 846, 356–391.

Rossinelli, D., Hejazialhosseini, B., Van Rees, W., Gazzola, M., Bergdorf, M., Koumoutsakos, P., 2015. MRAG-I2D: Multi-resolution adapted grids for remeshed vortex methods on multicore architectures. Journal of Computational Physics 288, 1–18.

Schnipper, T., Andersen, A., Bohr, T., 2009. Vortex wakes of a flapping foil. Journal of Fluid Mechanics 633, 411–423.

Shankar, S., Van Dommelen, L., 1996. A new diffusion procedure for vortex methods. Journal of Computational Physics 127 (1), 88–109.

Sun, P., Colagrossi, A., Marrone, S., Antuono, M., Zhang, A., 2018. Multi-resolution Delta-plus-SPH with tensile instability control: Towards high Reynolds number flows. Computer Physics Communications 224, 63–80.

Ye, H., Wei, H., Huang, H., Lu, X.-y., 2017. Two tandem flexible loops in a viscous flow. Physics of Fluids 29 (2), 021902.

Yokota, R., Barba, L., 2013. FMM-based vortex method for simulation of isotropic turbulence on gpus, compared with a spectral method. Computers & Fluids 80, 17–27.